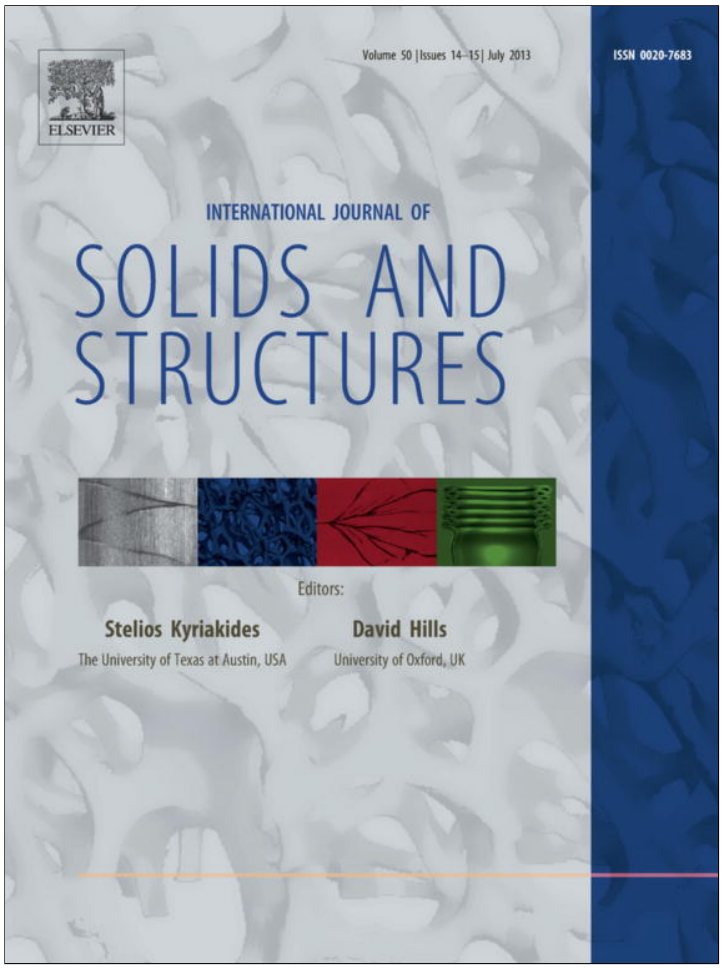

International Journal of Solids and Structures 50 (2013) 2115–2131

Contents lists available at SciVerse ScienceDirect

International Journal of Solids and Structures

journal homepage: www.elsevier.com/locate/ijsolstr

A yield function for single crystals containing voids

X. Han [a,b], J. Besson [a], S. Forest [a,*], B. Tanguy [b], S. Bugat [c]

[a] Centre des Matériaux, Mines ParisTech, CNRS UMR 7633, BP 87, 91003 Evry cedex, France
[b] Laboratoire de Comportement mécanique des Matériaux Irradiés, CEA Saclay, 91191 Gif-sur-Yvette cedex, France
[c] EDF R&D - Neutronic, NICT, Scientific Calculations Department, 1 avenue du General de Gaulle 92141 Clamart, France

ARTICLE INFO

Article history:
Received 16 May 2012
Received in revised form 27 October 2012
Available online 19 March 2013

Keywords:
Porous media
Single crystal
Variational approach
Yield criterion
Unit cell model

ABSTRACT

A yield function for single crystals containing voids has been developed based on a variational approach. This first yield function is phenomenologically extended by modifying the dependence on the mean stress and introducing three adjustable parameters. Unit cell finite element calculations are performed for various stress triaxiality ratios, main loading directions and porosity levels in the case of a perfectly plastic FCC single crystal. The three model parameters are adjusted on the unit cell calculations so that a very good agreement between simulation results and the proposed model is obtained.

1. Introduction

In crystalline metals, void nucleation, growth and coalescence lead to ductile fracture. Since the last forty years, building on the earliest works by Mc Clintock (1968); Rice and Tracey (1969); and Gurson (1977), much effort has been made to improve the prediction of damage evolution and fracture of porous ductile materials at macro and mesoscopic scales. The role of various characteristic features such as porosity, viscoplasticity, void shape, plastic anisotropy of the matrix has been studied. Some reviews were recently provided by Pineau and Pardoen (2007); Besson (2010); Benzerga and Leblond (2010). Two main approaches have been proposed to develop models for ductile damage growth. The first one is based on the seminal work by Gurson (1977) which uses an upper bound approach, following Tvergaard and Needleman (1984), Gologanu and Leblond (1993), Leblond et al. (1994), Benzerga and Besson (2001), Monchiet et al. (2007), Monchiet et al. (2008). The second approach is based on variational formulation of the homogenization theory using the concept of linear-comparison material, see Ponte Castañeda (1991); DeBotton and Ponte Castañeda (1995); Liu et al. (2005); Danas and Ponte Castañeda (2009) and Lebensohn et al. (2011).

Theoretical results obtained following these approaches can be verified using unit cell calculations first introduced in the pioneering work by Koplik and Needleman (1988). This versatile methodology allows to easily study the effect of various parameters on void growth and coalescence such as hardening rate (Faleskog et al., 1998; Gao et al., 1998; Lecarme et al., 2011), void shape or cell shape (Pardoen and Hutchinson, 2000), void population (Faleskog and Shih, 1997,Fabrègue and Pardoen, 2008 and Fritzen et al., 2012), void distribution (Bandstra and Koss, 2008), and second phase particles (Steglich and Brocks, 1997; Steglich et al., 1999).

The effect of the anisotropy of matrix behaviour on void growth was investigated in relation to the anisotropic plastic properties of metal sheets, see in particular (Benzerga et al., 2004) and more recently (Monchiet et al., 2008). Typically, a Hill-type yield criterion was assumed for the matrix in the latter references. The situation is quite different in the presence of voids embedded in a single crystalline matrix. The case of single crystals containing voids (hereafter referred to as porous single crystals) has only been studied recently using the unit cell methodology either based on FE simulations (Schacht et al., 2003; Yerra et al., 2010; Ha and Kim, 2010), or based on slip line theory in the case of simple cylindrical voids (Kysar et al., 2005; Gan et al., 2006; Gan and Kysar, 2007). Besides, the analysis of ductile fracture in single crystals has been performed at smaller scales for nano and micro-voids by means of Discrete Dislocations Dynamics in (Huang et al., 2007; Hussein et al., 2008; Segurado and Llorca, 2009; Segurado and Llorca, 2010 and Huang et al., 2012), and Molecular Dynamics in (Potirniche et al., 2006; Zhao et al., 2009; Traiviratana et al., 2008; Tang et al., 2010b and Tang et al., 2010a). However a set of constitutive equations describing the overall behaviour of porous single crystals is still lacking in the literature. The previously mentioned papers do

* Corresponding author at: Centre des Matériaux, Mines ParisTech, UMR CNRS 7633, BP 87, 91003 Evry cedex, France.
E-mail address: samuel.forest@ensmp.fr (S. Forest).

0020-7683/$ - see front matter © 2013 Published by Elsevier Ltd.
http://dx.doi.org/10.1016/j.ijsolstr.2013.02.005

not provide an overall yield function for porous single crystals. There is currently a real need for such a yield function that would be simple enough to allow straightforward Finite Element implementation for carrying out structural computations of ductile fracture in single and poly-crystals. It could be used for instance to reproduce experimental facts showing accelerated anisotropic growth of cavities in single crystals as observed in Crépin et al. (1996).

The purpose of the present work is to develop a model to describe the yield function of porous single crystals. Such models could be used to represent ductility of stainless steel (304/316 series) used for core internals of Fast Breeder Reactor and PWR nuclear power plants in which intragranular voids develop and lead to the phenomenon of swelling due to high irradiation levels (Foster and Strain, 1974; Seran et al., 1984; Dubuisson, 2011 and Renault et al., 2011), also that of Ni based single crystal superalloys used in turbo-engines components (Wang et al., 2006). The model is theoretically motivated using a micromechanical analysis based on the variational approach by (Ponte Castañeda and Suquet, 1998). It is extended on a phenomenological basis to match trends obtained for rate-independent material (e.g. Gurson–Tvergaard–Needleman model). Unit cell calculations are used to adjust and validate the model. Various loading directions and porosity levels (from 0.5% to 10%) are used.

The single crystal constitutive framework is recalled in Section 2.1. The proposed yield function for porous single crystal is presented in Section 2.2. The Section 3 is dedicated to the identification methodology of the corresponding material parameters from unit cell computations. The results and validation of the approach are provided in Section 4 in terms of crystal orientation, loading conditions and void volume fraction. The micromechanical motivation of the model is explained in Appendix A.

2. Proposed model for porous single crystals

The analysis given in this paper is limited to the small deformation framework, as it is the case in standard limit analysis.

2.1. Model for the single crystal matrix

In this work, which essentially deals with yielding of porous single crystals, a very simple law is used to describe the constitutive behaviour of the single crystal matrix. For each slip system $s = 1 \dots N$, the resolved shear stress, τ_s is expressed as:

$$\tau_s = \underline{\sigma} : \underline{m}_s \quad \text{with } \underline{m}_s = \frac{1}{2}\left(\vec{l}_s \otimes \vec{n}_s + \vec{n}_s \otimes \vec{l}_s\right) \tag{1}$$

where $\underline{\sigma}$ is the Cauchy stress tensor acting on the single crystal volume element. $\vec{l}_s$ and $\vec{n}_s$ are the unit vectors along the slip direction of the slip system s and normal to the slip plane, respectively. The total number of slip systems is N. For each slip system a yield surface can be defined as:

$$\psi_s = |\tau_s| - \tau_0 \tag{2}$$

Provided that $\psi_s \geqslant 0$, the slip rate for each slip system s is given as:

$$\dot{\gamma}_s(\tau_s) = \dot{\gamma}_0\left(\frac{\psi_s}{\tau_0}\right)^n = \dot{\gamma}_0\left(\frac{|\tau_s| - \tau_0}{\tau_0}\right)^n \tag{3}$$

where $\dot{\gamma}_0, \tau_0$ and n are material parameters. τ_0 represents the critical resolved shear stress (CRSS) of the slip system. For the sake of simplicity each slip system is assumed to have the same CRSS but the model presented here can be easily extended in order to take into account different CRSS as well as self and cross hardening. Using the normality rule, the plastic strain rate tensor, $\underline{\dot{\varepsilon}}_p$, is expressed as:

$$\underline{\dot{\varepsilon}}_p = \sum_s \dot{\gamma}_s \frac{\partial \psi_s}{\partial \underline{\sigma}} = \sum_s \dot{\gamma}_s \text{sign}(\tau_s)\underline{m}_s \tag{4}$$

2.2. Model for the porous single crystal

One considers here a single crystal containing spherical voids. The void volume fraction is referred to as f in the following. Based on the variational formulation proposed by Ponte Castañeda and Suquet (1998), it is shown in Appendix A that an effective scalar resolved stress acting on each slip system $\tau_s^*(\underline{\sigma}, f)$ can be defined as a function of the applied stress and the porosity level, such that:

$$\tau_s^* - \frac{1}{1-f}\left(\tau_s^2 + \frac{2}{45}f\sigma_{eq}^2 + \frac{3}{20}f\sigma_m^2\right)^{\frac{1}{2}} \overset{\text{def.}\tau_s^*}{=} 0 \tag{5}$$

where σ_m (resp. σ_{eq}) is the mean stress (resp. von Mises stress) of the macroscopic stress tensor $\underline{\sigma}$. τ_s^{*2} is expressed as a quadratic form of $\underline{\sigma}$. Note that the notations used here for the overall yield functions are different from those in Appendix A: Small letters are used for the stress and strain quantities instead of capital letters, because there is no reference any more to the micromechanical variational analysis. Similar yield functions were obtained in the case of a voided solid made of an isotropic von Mises matrix (Leblond et al., 1994). The quadratic dependence in (5) is known to be inadequate in the case of plastic solids since the seminal works of Mc Clintock (1968) and Rice and Tracey (1969). An exponential dependence on the mean stress should be preferred. Using the second order Taylor expansion of $\cosh(x) = 1 + \frac{1}{2}x^2$, other definitions of the effective scalar resolved stress τ_s^* can be proposed so that it better corresponds to models derived from the Gurson (1977) model. Following the concept of a scalar stress measure (Besson et al., 2001), which can be explicitly or implicitly defined, another expression for τ_s^* can be worked out from the following expression which takes into account the mean stress dependence as in Gurson type models:

$$\left(\frac{\tau_s^2}{\tau_s^{*2}} + \frac{2}{45}f\frac{\sigma_{eq}^2}{\tau_s^{*2}}\right) + 2f\cosh\left(\sqrt{\frac{3}{20}}\frac{\sigma_m}{\tau_s^*}\right) - 1 - f^2 \overset{\text{def.}\tau_s^*}{=} 0 \tag{6}$$

τ_s^* is found by solving this equation. Another solution, based on the recent development by Monchiet et al. (2007) would be to define τ_s^* based on the following equation:

$$\frac{\tau_s^2}{\tau_s^{*2}} + 2f\cosh\left(\sqrt{\frac{3}{20}\frac{\sigma_m^2}{\tau_s^{*2}} + \frac{2}{45}\frac{\sigma_{eq}^2}{\tau_s^{*2}}}\right) - 1 - f^2 \overset{\text{def.}\tau_s^*}{=} 0 \tag{7}$$

In the following the Gurson-like formulation will be used (Eq. 6). It is however well known that the original Gurson (1977) model could not well represent the behaviour of actual voided cells as simulated using finite element calculations (Brocks et al., 1995; Kuna and Sun, 1996 and Fritzen et al., 2012) so that empirical modifications have to be introduced to better represent the cell behaviour (Tvergaard and Needleman, 1984 and Faleskog et al., 1998). Accordingly, the following definition for τ_s^* is proposed:

$$\left(\frac{\tau_s^2}{\tau_s^{*2}} + \alpha\frac{2}{45}f\frac{\sigma_{eq}^2}{\tau_s^{*2}}\right) + 2q_1 f\cosh\left(q_2\sqrt{\frac{3}{20}}\frac{\sigma_m}{\tau_s^*}\right) - 1 - q_1^2 f^2 \overset{\text{def.}\tau_s^*}{=} 0 \tag{8}$$

where α, q_1 and q_2 are parameters that need to be adjusted. q_1 and q_2 play a similar role as in the work by Tvergaard and Needleman (1984) whereas α is a new parameter weighting the relative contribution of the resolved shear stress on each slip system and the usual isotropic equivalent von Mises stress measure. The identification of these parameters will be done in the following based on unit cell simulations of voided single crystals. In all cases, $\tau_s^* = |\tau_s|$ for $f = 0$ so that the yield surface of the single crystal matrix is retrieved.

For each slip system, the yield surface is then defined as:

$$\psi_s^* = \tau_s^* - \tau_0 = 0 \tag{9}$$

The plastic strain rate tensor is still expressed using the normality rule as:

$$\underline{\dot{\varepsilon}}_p = (1-f)\sum_s \dot{\gamma}_s \frac{\partial \psi_s^*}{\partial \underline{\sigma}} = (1-f)\sum_s \dot{\gamma}_s \frac{\partial \tau_s^*}{\partial \underline{\sigma}} \tag{10}$$

where $\dot{\gamma}_s$ is obtained as a function of τ_s^* using Eq. 3 as:

$$\dot{\gamma}_s(\tau_s) = \dot{\gamma}_0 \left(\frac{\psi_s^*}{\tau_0}\right)^n = \dot{\gamma}_0 \left(\frac{\tau_s^* - \tau_0}{\tau_0}\right)^n \tag{11}$$

Whatever the chosen definition (Eqs. (5)–(7) or 8), the effective stress τ_s^* is an homogeneous function of $\underline{\sigma}$ of degree 1 and differentiable so that (Euler's theorem): $\partial \tau_s^* / \partial \underline{\sigma} : \underline{\sigma} = \tau_s^*$. The plastic dissipation is obtained as:

$$\underline{\dot{\varepsilon}}_p : \underline{\sigma} = (1-f)\sum_s \dot{\gamma}_s \frac{\partial \tau_s^*}{\partial \underline{\sigma}} : \underline{\sigma} = (1-f)\sum_s \dot{\gamma}_s \tau_s^* \geqslant 0 \tag{12}$$

which expresses the equality between the plastic work at the macroscopic level (left-hand side) and the microscopic level (right-hand side). The factor $(1-f)$ on the right-hand side corresponds to the volume fraction occupied by the single crystal matrix in which a power equal to $\sum_s \dot{\gamma}_s \tau_s^*$ is dissipated.

3. Model parameter determination based on finite element analysis

In this section, the proposed model (Eq. 8) will be tested and adjusted. Finite element calculations of voided unit cells are carried out. The adjustable model parameters (α, q_1 and q_2) will be identified to represent unit cell calculations results. In this work Face-Centered Cubic (FCC) single crystals are considered. In this highly-symmetric crystalline structure, plastic slip occurs on a group of 12 slip systems following $\{111\}\langle 110\rangle$ (see Table 1). Eq. 11, which relates the slip rate to the effective resolved stress, can be rewritten as:

$$\tau_s^* - \tau_0 - \tau_0 \left(\frac{\dot{\gamma}_s}{\dot{\gamma}_0}\right)^{\frac{1}{n}} = 0 \tag{13}$$

In the limiting case of a nearly perfectly plastic behaviour, which is used in this study, calculations are performed such that the viscous stress is less than 1% of the CRSS:

$$\tau_0 \left(\frac{\dot{\gamma}_s}{\dot{\gamma}_0}\right)^{\frac{1}{n}} < 1\% \times \tau_0 \tag{14}$$

within the usual range of imposed strain rates for engineering materials.

The material parameters for a FCC single crystal used for the unit cell analysis are given in Table 2. The elastoviscoplastic crystal plasticity model based on Schmid's law with a threshold requires the choice of elasticity moduli. The elastic moduli (cubic elasticity C_{11}, C_{12} and C_{44}) take here typical values for 300 series austenitic stainless steels at 340°C. However, as it is well-known in porous plasticity, the results of the limit analysis do not depend on the elastic properties of the material but only on the plasticity threshold value. This has been checked for unit cell computations with a single void but also for populations of interacting voids, for instance in Fritzen et al. (2012). The same feature has been checked here for crystal plasticity in the presented unit cell computations. The value of the parameter $\dot{\gamma}_0$ is chosen to satisfy the condition given in Eq. 14. The same threshold value $\tau_0 = 60$ MPa is considered for all slip systems in Schmid's law. Accordingly, activation of one slip system at a given Gauss point of the finite element mesh depends on the value of the resolved shear stress at this point. The 12 possible slip systems are considered at each material point. In the simulation, slip system activation is heterogeneous due to the presence of the hole. Multiple slip is allowed and takes place at several locations. Fully-implicit time integration method is used for the material's constitutive equations (Foerch et al., 1997).

Table 2
Material parameters for FE simulations.

C_{11}	C_{12}	C_{44}	τ_0	n	$\dot{\gamma}_0$
199 GPa	136 GPa	105 GPa	60 MPa	5	7.776 10^8 s^{-1}

3.1. 3D finite element unit cell model

In the last decades, the FE simulation of unit cells has become a well-known simulation technique to investigate the global and local responses of heterogeneous materials (Needleman, 1972; Tvergaard, 1981; Tvergaard, 1982; Koplik and Needleman, 1988; Worswick and Pick, 1990; Quinn et al., 1997; Pardoen and Hutchinson, 2000 and Benzerga and Besson, 2001). Three-dimensional unit cell calculations of porous media, considered as an homogenization method of a representative volume element (RVE) containing uniformly distributed voids, are widely applied to study the effect of various parameters such as multiaxial stress state, crystallographic orientation, and initial void volume fraction, on void growth (Liu et al., 2007; Yerra et al., 2010; Ha and Kim, 2010 and Yu et al., 2010) and coalescence (Kuna and Sun, 1996,Zhang et al., 1999,Schacht et al., 2003,Liu et al., 2007,Liu et al., 2010,Yerra et al., 2010 and Liu et al., 2012).

In this study, FE simulation of unit cells is used to determine the yield surface of porous single crystals depending on crystallographic orientation and void volume fraction. Results of the simulation are used to calibrate the model parameters (q_1, q_2 and α) introduced in the previous section Eq. 8. The FE mesh used for the simulation is shown in Fig. 1. The cubic cell (length l_0) contains a spherical void (radius r_0) located at the center of the cell. Except for specific crystallographic orientation the problem has no symmetry so that the full cell has to be meshed. The void volume fraction is simply given by: $f = V_{void}/V_{tot} = \frac{4}{3}\pi r_0^3 / l_0^3$.

The 3D mesh is made of reduced-integrated quadratic hexahedral elements (see Fig. 1). The simulations were carried out using the Zset FE software (Besson and Foerch, 1998). A convergence study was also performed to optimize calculation time while keeping sufficient accuracy. Calculations are carried out so as to prescribe a constant overall stress triaxiality ratio (ratio of the mean stress to the von Mises stress). The overall macroscopic stress tensor is expressed in terms of 3 principal stresses as:

$$\underline{\sigma} = \begin{bmatrix} \sigma_1 & 0 & 0 \\ 0 & \sigma_2 & 0 \\ 0 & 0 & \sigma_3 \end{bmatrix} = \sigma_1 \begin{bmatrix} 1 & 0 & 0 \\ 0 & \eta_2 & 0 \\ 0 & 0 & \eta_3 \end{bmatrix} \tag{15}$$

Table 1
Slip systems in FCC single crystals.

Slip system s	1	2	3	4	5	6	7	8	9	10	11	12
Slip plane $\vec{n}$		(111)			$(1\bar{1}1)$			$(\bar{1}11)$			$(11\bar{1})$	
Slip direction $\vec{l}$	$[\bar{1}01]$	$[0\bar{1}1]$	$[\bar{1}10]$	$[\bar{1}01]$	[011]	[110]	$[0\bar{1}1]$	[110]	[101]	$[\bar{1}10]$	[101]	[011]

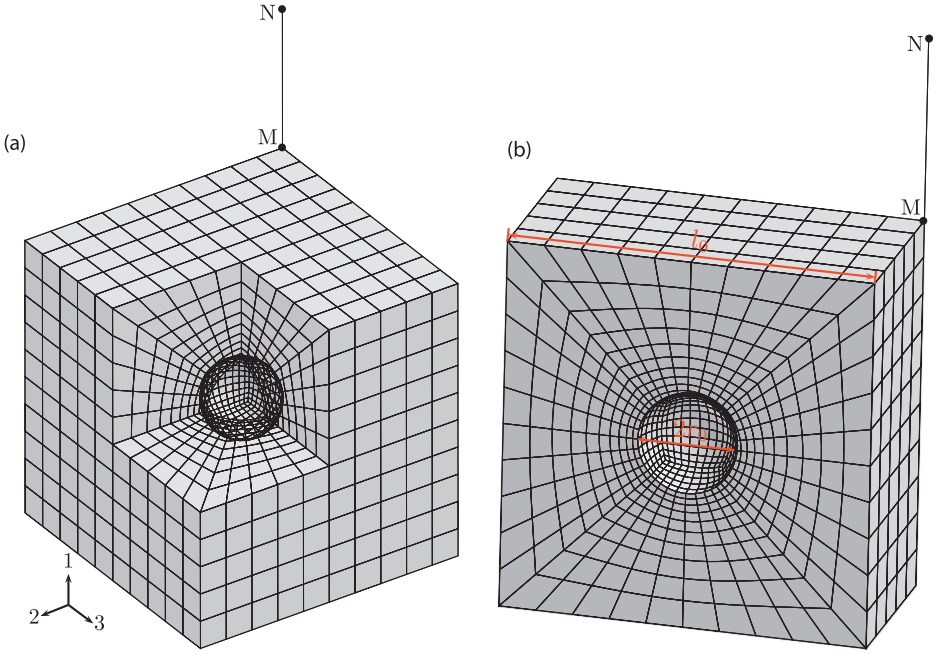

Fig. 1. Unit cell with a spherical void in its center. (a) FE mesh for $f = 0.01$, with a cut of 1/8 of the full geometry; (b) half of the full geometry showing the dimensions of the unit cell with a central void.

where η_2 and η_3 are loading parameters which are kept constant for every single unit cell simulation. Both parameters vary between -0.5 and 1. It is assumed that $\sigma_1 > 0$. The stress triaxiality ratio is expressed as:

$$a = \frac{\sigma_m}{\sigma_{eq}} = \frac{1 + \eta_2 + \eta_3}{3\sqrt{1 - \eta_2 - \eta_3 - \eta_2\eta_3 + \eta_2^2 + \eta_3^2}} \tag{16}$$

As triaxiality shall be kept constant during the loading history, the parameters η_2 and η_3 have to remain constant whereas the ratios of mean strains E_{22}/E_{11} and E_{33}/E_{11} will vary in time. Two strategies were used to prescribe constant triaxiality. The first one uses the technique presented by Brocks et al. (1995). A special truss element (MN in Fig. 1) is added to the mesh. It acts as a spring in the main loading direction (i.e. **1**) which measures the mean stress component in that direction. A portion (η_2 and η_3) of this stress is then applied in both other directions **2** and **3**. Normal displacements on the cell faces are kept homogeneous so that the cell keeps a parallelepidic shape. This technique allows to perform displacement controlled FE simulations. It is suitable for highly symmetric crystal directions (e.g. $\mathbf{1} = [100], \mathbf{2} = [010], \mathbf{3} = [001]$) but tends to overconstrain the model for general orientations so that high stresses are generated (in some cases stresses higher than the theoretical stresses for the undamaged single crystal are obtained). For this reason a second simulation technique assuming periodic boundary conditions was also used. The displacement vector $\vec{u}$ associated with each material point $\vec{x}$ takes the form:

$$\vec{u} = \underline{E} \cdot \vec{x} + \vec{v}, \quad \forall \vec{x} \in V_{tot} \tag{17}$$

where $\underline{E}$ denotes the macroscopic strain tensor and $\vec{v}$ is the periodic fluctuation vector, which takes the same value for two points situated on opposite outer boundary surfaces ∂V_{tot} of the entire volume V_{tot}, while the traction vector $\vec{t} = \underline{\sigma} \cdot \vec{n}$ takes opposite values on these two points, with $\vec{n}$ being the outer unit normal vector on ∂V_{tot}. In the finite element implementation, the components of the macroscopic strain tensor, E_{ij}, are degrees of freedom and the associated reactions of which, R_{ij}, correspond to the macroscopic stress component Σ_{ij} times the cell volume: $R_{ij} = V_{tot} \times \Sigma_{ij}$, see (Besson et al., 2009). Simulations are then carried out prescribing the different reactions so that $R_{22} = \eta_2 R_{11}, R_{33} = \eta_3 R_{11}$ and $R_{12} = R_{23} = R_{31} = 0$. In that case, simulations are load controlled.

Both methods (spring loaded cell and fully periodic cell) were compared in the case of highly symmetric triaxial loading (e.g. [100]–[010]–[001]). Results shown in Fig. 2 indicate that both methods result in almost identical results in this particular case. In the general case of non-symmetric orientations, spring loading conditions lead to an over-constraining effect so that slightly larger yield surfaces are generated. It is also shown that the stress levels quickly stabilize (due to the absence of work hardening). Based on these results, stress levels used to calibrate and validate the proposed yield function will be determined for a strain along direction **1** equal to 3%.

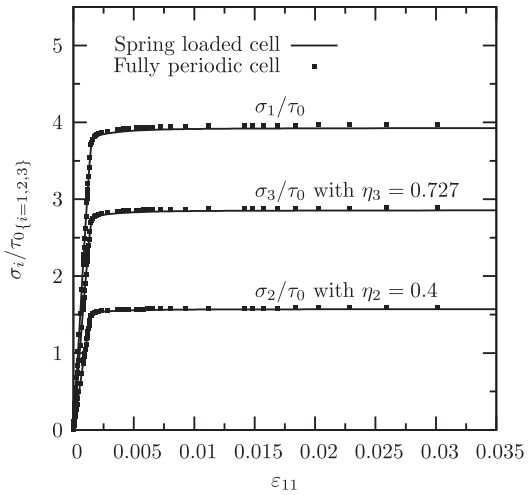

Fig. 2. Normalized macroscopic stresses along the three principal loading directions as functions of the macroscopic deformation along direction **1** for $\mathbf{1} = [100], \mathbf{2} = [010]$ and $\mathbf{3} = [001]$ with $\eta_2 = 0.4, \eta_3 = 0.727$ and a porosity level $f = 0.01$.

3.2. Model parameter determination

In order to identify the model parameters from various numerical simulations for different crystallographic orientations, the proposed model can be written as:

$$\left(\frac{\left(\left(\underline{P}^T\cdot\underline{\sigma}\cdot\underline{P}\right):\underline{m}_s\right)^2}{\tau_s^{*2}}+\alpha\frac{2f}{45}\frac{\sigma_{eq}^2}{\tau_s^{*2}}\right)+2q_1f\cosh\left(q_2\sqrt{\frac{3}{20}}\frac{\sigma_m}{\tau_s^*}\right)-1-(q_1f)^2\overset{\text{def.}\tau_s^*}{=}0 \tag{18}$$

where $\underline{\sigma}$ is the macroscopic stress tensor on global coordinates defined in Eq. 15 and $\underline{P}$ denotes the rotation matrix following **zxz** convention (Goldstein et al., 2002), which turns global basis to crystal basis using Euler angles (ϕ_1,Φ,ϕ_2), given by:

$$\underline{P}=\begin{bmatrix}\cos\phi_1\cos\phi_2-\sin\phi_1\cos\Phi\sin\phi_2 & \sin\phi_1\cos\phi_2+\cos\phi_1\cos\Phi\sin\phi_2 & \sin\Phi\sin\phi_2\\ -\cos\phi_1\sin\phi_2-\sin\phi_1\cos\Phi\cos\phi_2 & -\sin\phi_1\sin\phi_2+\cos\phi_1\cos\Phi\cos\phi_2 & \sin\Phi\cos\phi_2\\ \sin\phi_1\sin\Phi & -\cos\phi_1\sin\Phi & \cos\Phi\end{bmatrix} \tag{19}$$

To validate the proposed model for single crystals, five crystallographic orientations for the main loading direction (direction **1**) have been chosen: $[100],[110],[111],[210]$ and $[\bar{1}25]$. Another three cases are complemented to study the effect of secondary loading directions (directions **2** and **3**). All these cases are summarized in Table 3. Five porosity levels are considered as follows: $f=0.005$, 0.01, 0.02, 0.05 and 0.1.

Note that a special case with axisymmetric triaxial stress state $(\eta_2=\eta_3=\eta)$ will also be investigated. In that case the stress triaxiality ratio is expressed as: $a=\frac{1}{3}(1+2\eta)/(1-\eta)$. The orthogonality of the three imposed principal stresses, the axisymmetric stress state and the symmetric crystalline structure of FCC materials allow deriving a simplified expression of the resolved shear stress on slip system s, which is then expressed as:

$$|\tau_s|=\left|\left(\underline{P}^T\cdot\underline{\sigma}\cdot\underline{P}\right):\underline{m}_s\right|=F_s^{\mathbf{1}}\sigma_{eq}=F_s^{\mathbf{1}}(1-\eta)\sigma_1 \tag{20}$$

where $F_s^{\mathbf{1}}$ is the Schmid factor for slip system s obtained from a uniaxial tensile test on the matrix material along the main loading

Table 3
Crystallographic orientations for numerical simulations and corresponding Euler angles.

Test number	Crystallographic orientation on global coordinates 1-2-3	Euler angles (°)		
		ϕ_1	Φ	ϕ_2
1	[100]-[010]-[001]	0	0	0
2	[100]-[01$\bar{1}$]-[011]	180	45	180
3	[100]-[02$\bar{1}$]-[012]	180	26.57	180
4	[110]-[$\bar{1}$10]-[001]	45	0	0
5	[111]-[$\bar{2}$11]-[0$\bar{1}$1]	0	45	54.74
6	[210]-[$\bar{1}$20]-[001]	26.57	0	0
7	[$\bar{1}$25]-[1$\bar{2}$1]-[210]	116.57	90	65.91
8	[$\bar{1}$25]-[0$\bar{5}$2]-[(29)25]	93.95	80.24	67.86

Table 6
Adjusted values of model parameters.

α	q_1	q_2
6.456	1.471	1.325

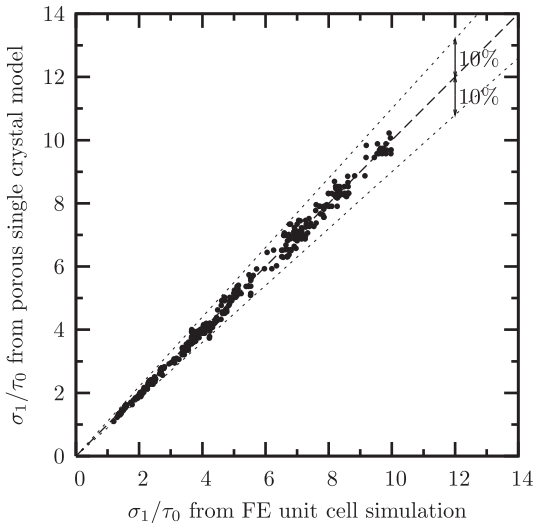

Fig. 3. Identification results showing comparison points between FE unit cell simulations and effective single crystal model predictions. They are contained in a 10% error cone.

Table 4
Triaxialities applied for FE simulations and values of corresponding model parameter η.

a	0	0.33	0.5	1.0	1.5	3.0	5.0	10.0	50.0	$+\infty$
η	−0.5	0	0.143	0.4	0.538	0.727	0.824	0.906	0.980	1.0

Table 5
List of all the performed unit cell FE calculations.

Test details	Number of tests	Figures
8 orientations $f=0.01\times$ (4 × 10 FE calculations−3redundant tests)	$8\times(4\times10-3)=296$	4–14
4 porosities × 3 orientations ×10 FE calculations	$4\times3\times10=120$	16
$f=0.005, f=0.02,\times$ 2 orientations [110] and [210] ×10 FE calculations	$2\times2\times10=40$	none[1]

[1] used only for parameter identification.

direction **1**. Hence, the resulting effective resolved stress τ_s^* for slip system s is given by:

$$\left(\left(F_s^{\mathbf{1}}\right)^2+\alpha\frac{2f}{45}\right)\frac{(1-\eta)^2\sigma_1^2}{\tau_s^{*2}} + 2q_1 f\cosh\left(\frac{q_2}{2}\sqrt{\frac{1}{15}}\frac{(1+2\eta)\sigma_1}{\tau_s^*}\right)-1-(q_1 f)^2 \overset{\text{def.}\tau_s^*}{=} 0 \qquad (21)$$

Based on this equation, the whole range of positive stress triaxiality from zero to infinity will be investigated. In FE simulations, ten distributed values of triaxialities have been chosen to test the proposed model (see Table 4).

A total number of 456 FE calculations were carried out and listed in Table 5, with above-mentioned triaxial stress states, crystallographic orientations and porosities. The loading conditions are characterized by η_2 and η_3. Four cases were considered successively: $\eta_2=\eta_3, \eta_2=0.4, \eta_2=0.727, \eta_2=1$. In each case, 10 values of η_3 were applied. The porosity $f=0.01$ was first considered for 8 crystallographic orientations. Four more porosities $f=0.005$, 0.02, 0.05 and 0.1 were considered, with 3 crystallographic orientations [001], [111] and [−125], and again 10 loading conditions. Additional tests are necessary to check the effect of porosity along other crystallographic orientations [011] and [210], for porosities $f=0.005$ and 0.02.

The details of these simulations results will be presented and discussed in the next section. The model parameters α, q_1 and q_2 have been identified by minimizing (Levenberg–Marquardt method) the quadratic difference between model results and FE unit cell

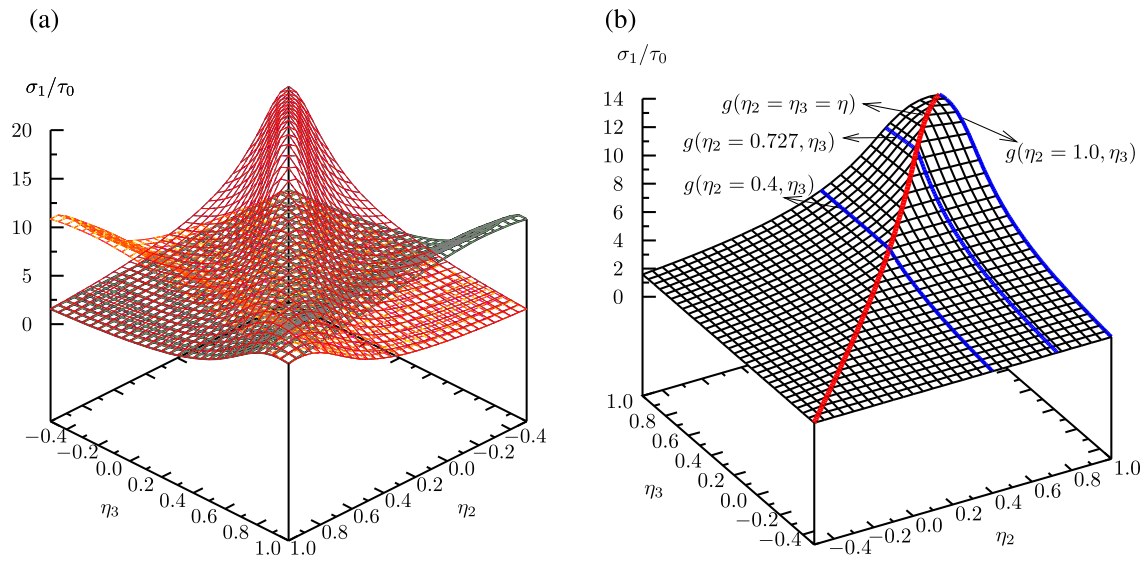

Fig. 4. 3D yield surfaces for [100] – [010] – [001] triaxial loading direction, with $f=0.01$. (a) Yield surfaces for each of the 12 slip systems; (b) Yield surface for the porous single crystal.

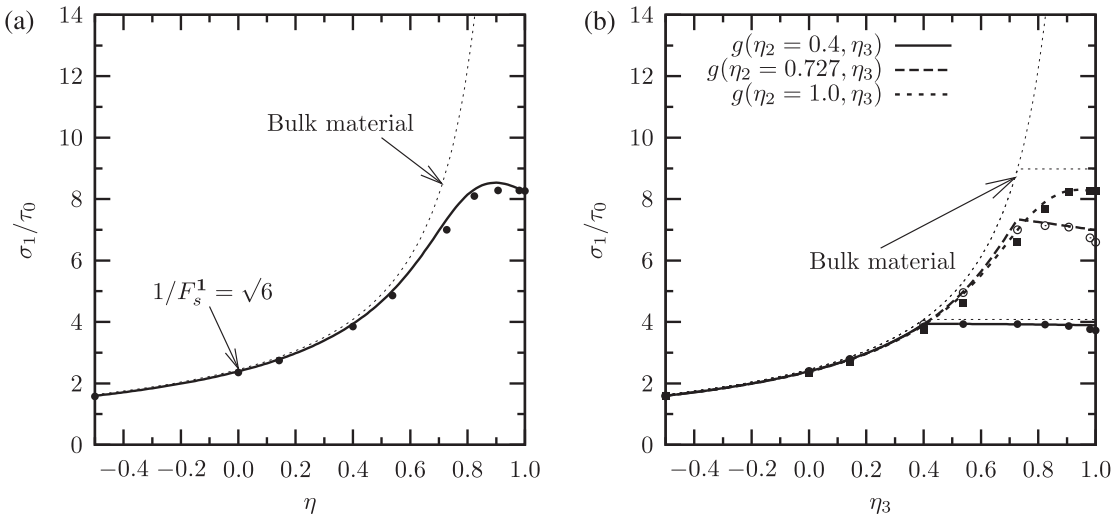

Fig. 5. Yield surfaces for [100] – [010] – [001] triaxial loading direction, with $f=0.01$. (a) Yield surface for the porous single crystal, with $\eta_2=\eta_3=\eta$ (*i.e.* red curve in Fig. 4b). (b) Yield surfaces for the porous single crystal, with η_2 respectively fixed to 0.4, 0.727 and 1.0 (*i.e.* blue curves in Fig. 4b). Thick continuous and dashed lines correspond to the yield surfaces for the proposed model. Symbols correspond to 3D unit cell FE analyses. Thin dashed lines correspond to the bulk material (non porous single crystal) obtained from the proposed model for each studied case.

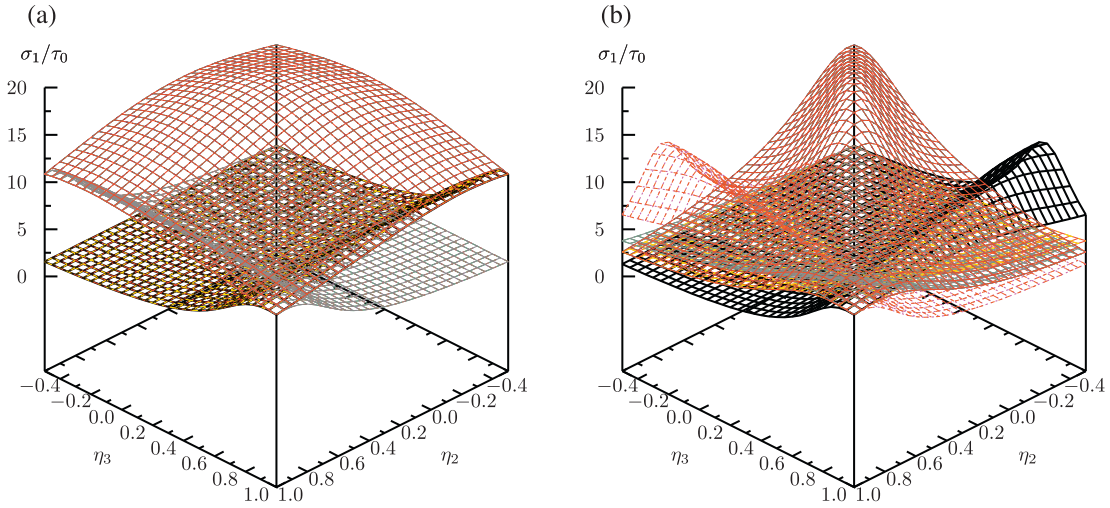

Fig. 6. 3D yield surfaces for each of the 12 slip systems, with $f = 0.01$: (a) for [100] – [01$\bar{1}$] – [011] triaxial loading direction; (b) for [100] – [02$\bar{1}$] – [012] triaxial loading direction.

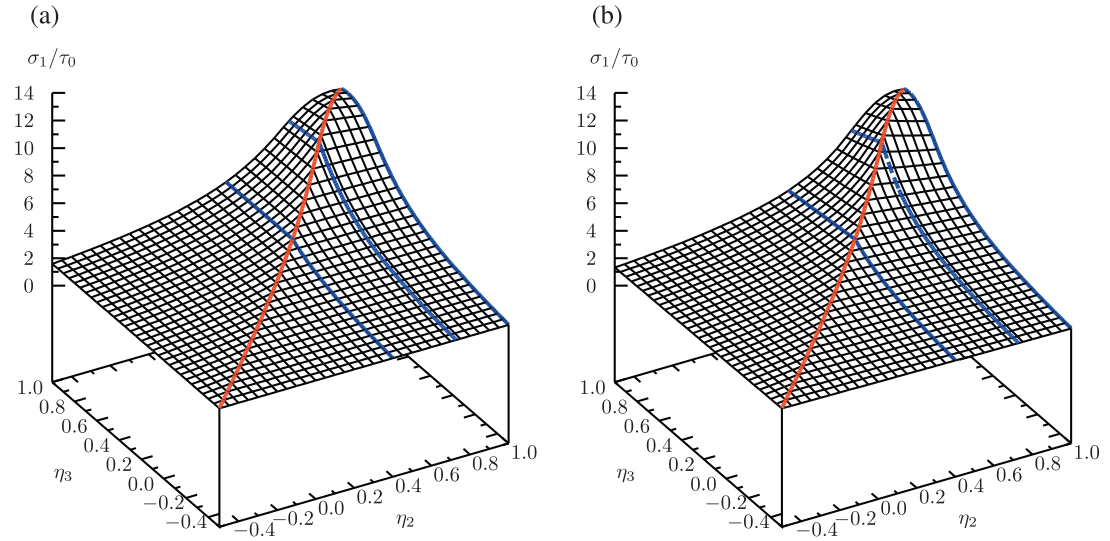

Fig. 7. Yield surfaces for the porous single crystal, with $f = 0.01$: (a) for [100] – [01$\bar{1}$] – [011] triaxial loading direction; (b) for [100] – [02$\bar{1}$] – [012] triaxial loading direction.

simulation results. Optimized values are given in Table 6. Comparison of these two sets of data after identification is shown in Fig. 3. The maximum error is always less than 10% and much smaller in many cases. Theoretical values for α, q_1 and q_2 are equal to 1 (see Eq. 6). The calibrated value for q_1 is close to 1.5 which is in agreement with the literature in the case of an isotropic von Mises matrix (see e.g. (Faleskog et al., 1998; Gao et al., 1998)). In particular a value for q_1 equal to 1.5 is very often used. The calibrated value for α is significantly higher than the theoretical one. Note that α plays an important role at high porosities (i.e. 5% and 10%).

4. Results and discussion

In this section, the model predictions and unit cell analyses are compared for specific cases in order to examine the effect of crystallographic orientation and porosity on the resulting yield surface. Note that, for the sake of a nearly perfectly plastic behaviour used in FE simulations, the limit surfaces obtained from limit analyses could be considered as a good estimation of the yield surfaces. Therefore, it was assumed that the limit surface is identical to the yield surface so that in this section the"yield surface" term would be used to describe these two material properties.

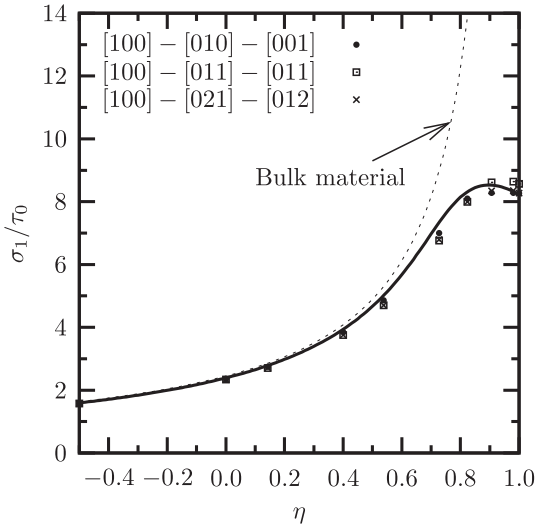

Fig. 8. Yield surfaces for [100] main loading direction, in the case with $\eta_2 = \eta_3 = \eta$, for various secondary loading directions, $f = 0.01$.

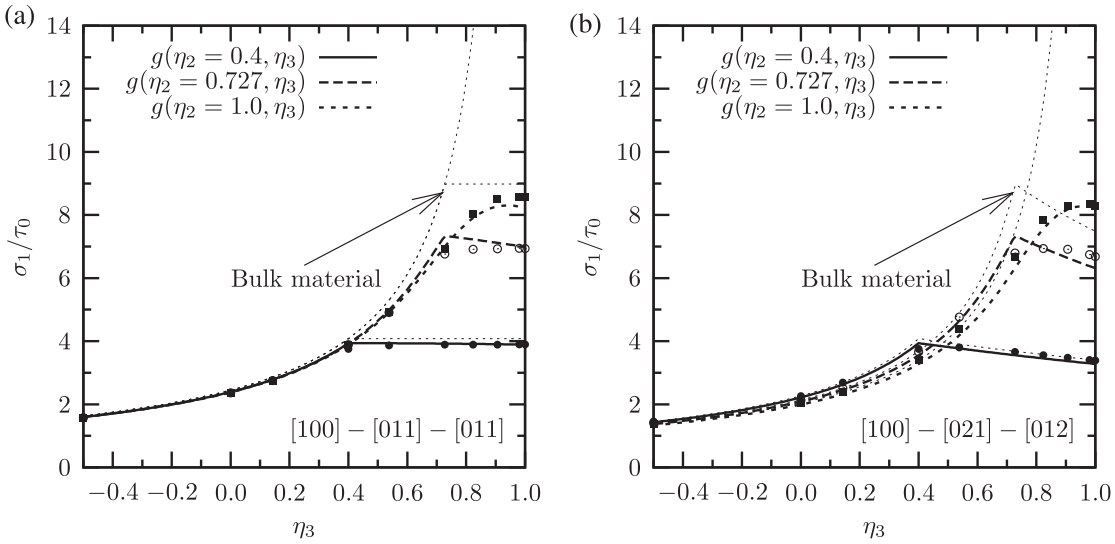

Fig. 9. Yield surfaces for the porous single crystal, in the cases of η_2 fixed at 0.4, 0.727 and 1.0, with $f = 0.01$: (a) for [100] – [01$\bar{1}$] – [011] triaxial loading direction; (b) for [100] – [02$\bar{1}$] – [012] triaxial loading direction.

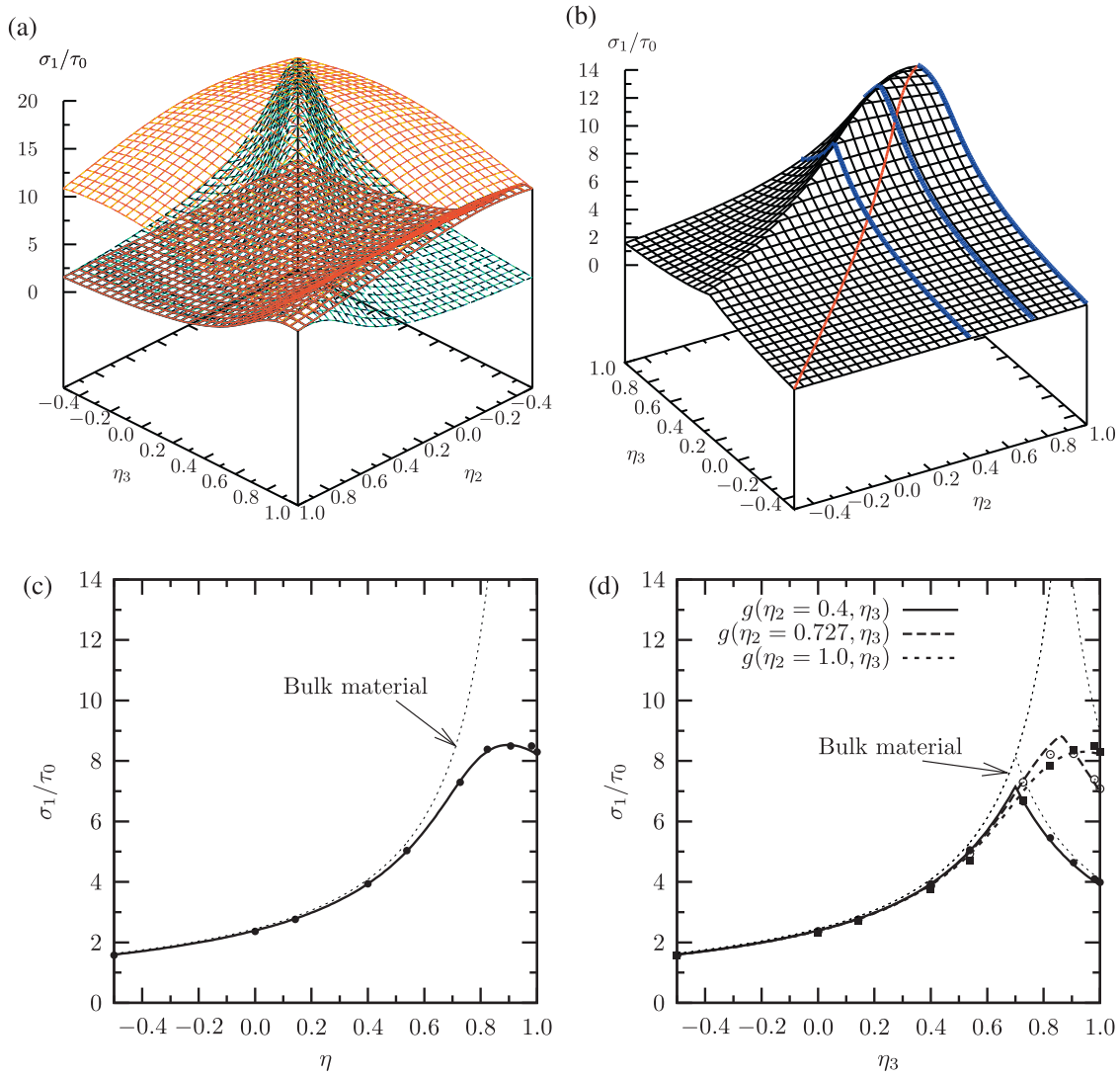

Fig. 10. Yield surfaces for [110] – [$\bar{1}$10] – [001] triaxial loading direction, with $f = 0.01$. (a) 3D yield surfaces for all 12 slip systems; (b) 3D yield surface for the porous single crystal. (c) Yield surface for the porous single crystal, with $\eta_2 = \eta_3 = \eta$; (d) Yield surfaces for the porous single crystal, with η_2 fixed at 0.4, 0.727 and 1.0.

4.1. Representation of the yield surface

The overall yield surface results, as in the case of a non porous single crystal, from the intersections of the yield surfaces (12 in the present case) for each individual slip system. It is therefore not possible to represent the macroscopic yield surface by expressing the von Mises stress as a function of the mean stress (i.e. $\sigma_{eq} = g(\sigma_m)$) as in the case of the Gurson model. In the following, the yield surface will be represented by plotting (3D plot) the macroscopic stress along the main loading direction **1** normalized by the CRSS, as a function of secondary loading parameters η_2 and η_3:

$$\sigma_1/\tau_0 = g(\eta_2, \eta_3) \tag{22}$$

In the case of axisymmetric loading (i.e. $\eta_2 = \eta_3 = \eta$), this normalized macroscopic stress is simply expressed as a function of η (2D plot) as:

$$\sigma_1/\tau_0 = g(\eta) \tag{23}$$

4.2. Results for [100]–[010]–[001] triaxial loading

In this section, the three triaxial loading directions (**1**, **2** and **3**) coincide with the ⟨100⟩ directions of the single crystal. The porosity is equal to 1%. The resulting theroretical 12 yield surfaces (Eq. 8) for all slip systems are plotted in Fig. 4a while Fig. 4b shows the overall yield surface resulting from the intersection of the individual yield surfaces. In that particular loading case, it is important to recall that the ⟨100⟩ loading direction family leads to the same projection of the stress vector on the four slip planes of a FCC cystal (see Table 1). For this symmetry reason, only three distinct groups of curves are obtained, which correspond to the three slip systems on each slip plane (see Fig. 4a). In particular, the yield surface of the single crystal is symmetric with respect to the $\eta_2 = \eta_3$ line. Four special loading cases to be closely investigated in the following are indicated by colored lines (red and blue lines) in Fig. 4b: (i) $\eta_2 = \eta_3 = \eta$, (ii) $\eta_2 = 0.4$, (iii) $\eta_2 = 0.727$ and (iv) $\eta_2 = 1$. Model results Eq. (8) are now compared to unit cell simulation results.

Results for the $\eta_2 = \eta_3$ case are compared in Fig. 5a. In that particular case, the resulting yield surface is differentiable. This corresponds to the fact that the same slip systems are activated for all loading conditions. For this highly symmetric case, two of the three slip systems of each slip plane play the same role and are consequently active (in total eight slip systems are active). For the same reason, similar results are also obtained for the $\eta_2 = 1$ case (i.e. $\sigma_1 = \sigma_2$) in Fig. 5b, but the active slip systems are different from that of the previous case. However, in cases with η_2 fixed to 0.4

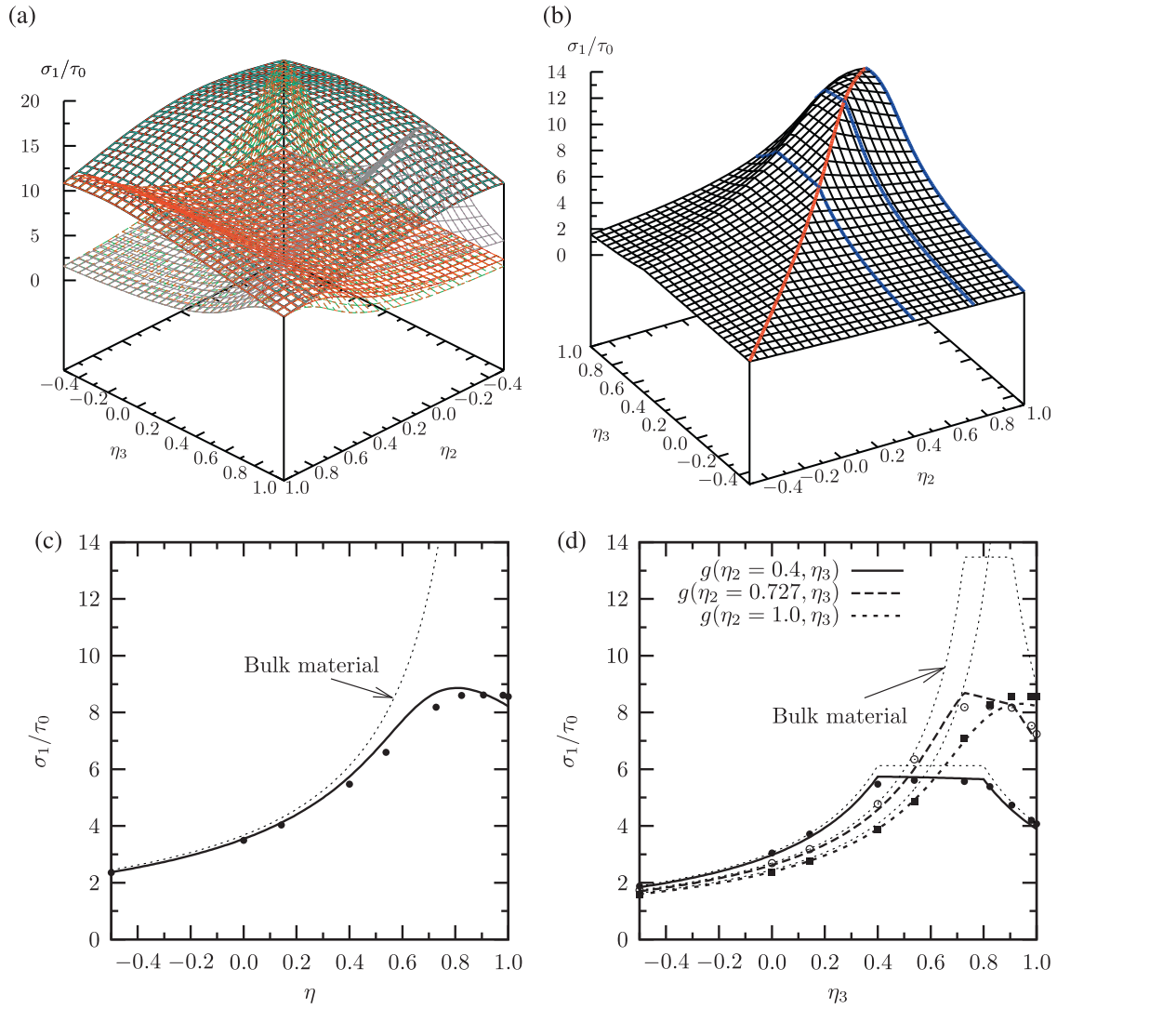

Fig. 11. Yield surfaces for [111] – [$\bar{2}$11] – [0$\bar{1}$1] triaxial loading direction, with $f = 0.01$. (a) 3D yield surfaces for all 12 slip systems; (b) 3D yield surface for the porous single crystal. (c) Yield surface for the porous single crystal, with $\eta_2 = \eta_3 = \eta$; (d) Yield surface for the porous single crystal, with η_2 fixed at 0.4, 0.727 and 1.0.

or 0.727 (Fig. 5b), two regimes are observed on the yield surface. In the case where $\eta_2 = 0.4$ (resp. $\eta_2 = 0.727$), only one slip system is active on each slip plane for η_3 between −0.5 and 0.4 (resp. 0.727). For η_3 above 0.4 (resp. 0.727), the active slip systems are replaced by different ones so that the resulting yield surface presents a discontinuous derivative at $\eta_3 = 0.4$ (resp. $\eta_2 = 0.727$). These evolutions are due to the behaviour of the matrix material only; one can note that similar trends are observed for the non-porous single crystal (called bulk material in the figures, see the thin dashed lines in Fig. 5).

In all these cases, the proposed model accurately captures the FE simulations over the whole range of investigated stress triaxialities. Note that due to the low porosity level (1%), results obtained for the porous crystal and the bulk material remain close except for high stress triaxialities. In particular $\sigma_1 \to \infty$ when $\eta_2 \to 1$ and $\eta_3 \to 1$ for the bulk material whereas σ_1 keeps finite values for the porous single crystal. On the other hand for pure tensile loading ($\eta_2 = \eta_3 = 0$), both model and simulation are close to the theoretical value for the bulk single crystal: $\sigma_1/\tau_0 \approx 1/F_s^{\mathbf{1}} = \sqrt{6}$ where $F_s^{\mathbf{1}}$ is the Schmid factor for [100] loading.

4.3. Effect of secondary loading direction: [100] − [0ij] − [0$\bar{j}$i]

The effect of the secondary loading direction on the yield surface of the porous single crystal is investigated for a fixed main loading direction **1** = [100]. The secondary loading direction **3** is set to [011] or to [012]. The yield surfaces for each effective slip system of the porous single crystal are illustrated respectively in Fig. 6a and b for these two cases. In the first case ([100] − [01$\bar{1}$] − [011]), just like in the reference case ([100]–[010]–[001]), the loading direction family ⟨011⟩ leads to the same Schmid factor for every activated slip system while for the other non-activated slip systems the Schmid factor is equal to zero. Moreover, the Schmid factors for ⟨100⟩ and ⟨110⟩ loading direction families have the same value ($F_s = \sqrt{6}/6$). For these reasons, only 3 groups of yield surfaces can be identified, and the yield surface of the overall porous single crystal (see Fig. 7a) presents exactly the same surface as in the reference case. However non-activated slip systems lead to different yield surfaces (compare Figs. 4a and 6a) so that the post-yield behaviour could be different in the case where the single crystal exhibits work-hardening.

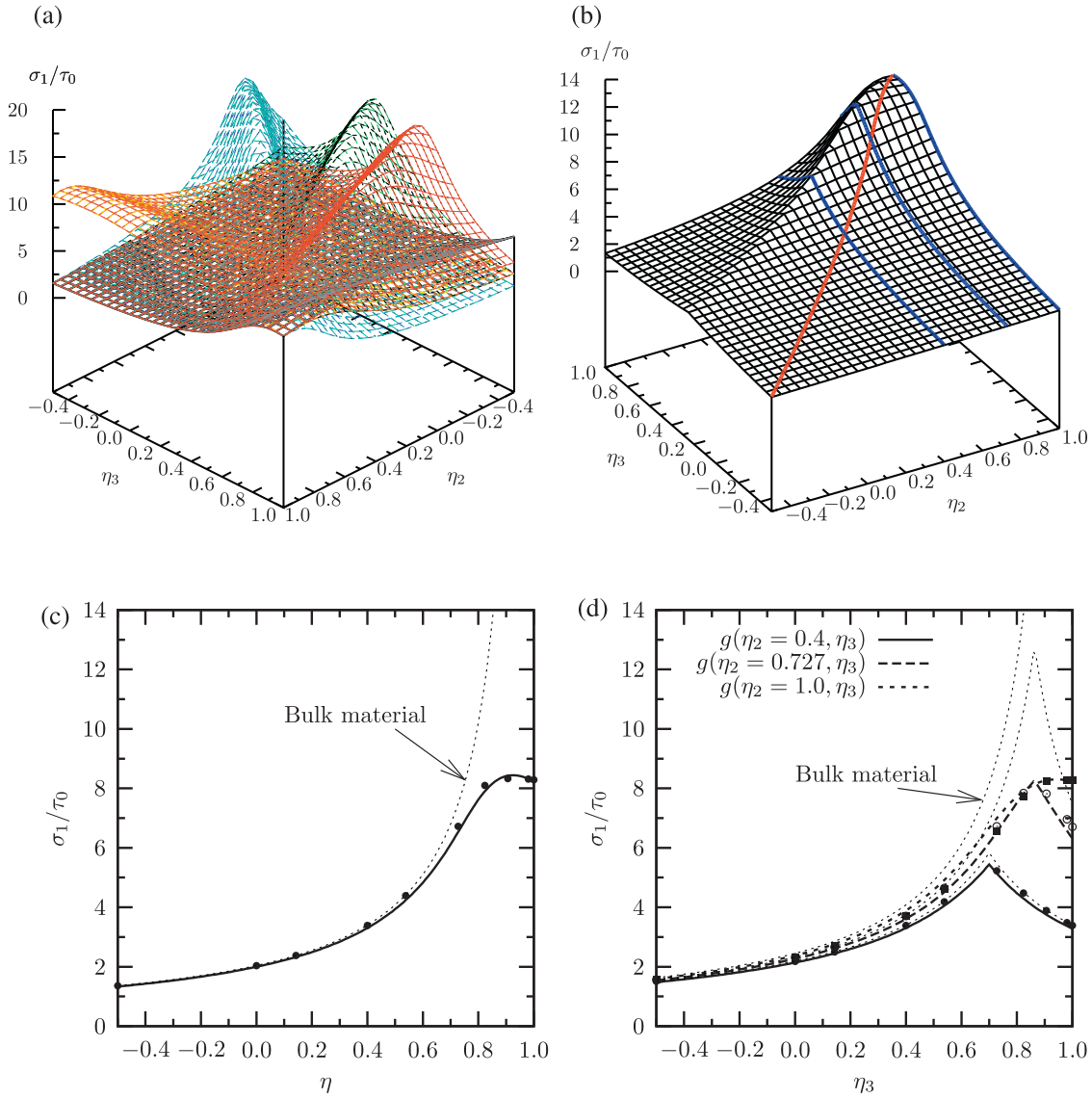

Fig. 12. Yield surfaces for [210] – [$\bar{1}$20] – [001] triaxial loading direction, with $f = 0.01$. (a) 3D yield surfaces for all 12 slip systems; (b) 3D yield surface for the porous single crystal. (c) Yield surface for the porous single crystal, with $\eta_2 = \eta_3 = \eta$; (d) Yield surface for the porous single crystal, with η_2 fixed at 0.4, 0.727 and 1.0.

In the second case ([100] – [02$\bar{1}$] – [012]), since the secondary loading direction does not lead to the same Schmid factor for every slip system, more numerous distinct yield surfaces are observed in Fig. 6b, and the yield surface for the porous single crystal in this case (Fig. 7b) is slightly different from the previous one.

Fig. 8 shows the yield surface predicted by the proposed model with corresponding data points calculated by FE method for $\eta_2 = \eta_3 = \eta$, for the same main loading direction [100] and different secondary loading directions. As shown from Eq. 21, the secondary loading directions do not affect the predicted yield surface in this particular diagonal case. In the case explored by Figs. 9a and b, with fixed values for η_2, the yield surfaces are slightly different while the proposed model is able to capture the FE simulation data with a good accuracy.

4.4. Effect of main loading direction

The effect of the main loading direction (**1**) is investigated in this section. Comparisons between results obtained by the proposed model and by FE unit cell simulations are shown for the following orientations [110] (see Fig. 10), [111] (see Fig. 11), [210] (see Fig. 12) and and finally [$\bar{1}$25] (see Fig. 13). In this last case, the effect of the secondary loading direction (**3**) is also studied.

Yield surfaces predicted by the model for main loading directions taken equal to [110], [111] or [210] significantly differ (see Figs. 10b, 11b and 12b). In comparison to the **1** = [100] case, yield surfaces are no longer symmetric with respect to the $\eta_2 = \eta_3$ line. As previously noted, the sharp slope changes on the yield surfaces correspond to a change in the active slip systems. These trends are directly due to the crystallographic nature of the matrix material. Due to the low porosity, the difference between the yield surface of the bulk material (see Figs. 10c/d, 11c/d and 12c/d) and that of the porous material is only significant at high stress triaxiality levels. In all cases, the model prediction and the FE unit cell results are in very good agreement (see Figs. 10c/d, 11c/d and 12c/d, model: lines, FE results: symbols).

All cases presented above exhibit some degree of symmetry so that several individual slip systems may have the same yield surface. In order to check the validity of the proposed model in cases where loading has little or no symmetry with respect to the crystallographic orientation, main loading along the [$\bar{1}$25] crystal direction was investigated. For **3** = [210], 11 different yield surfaces for

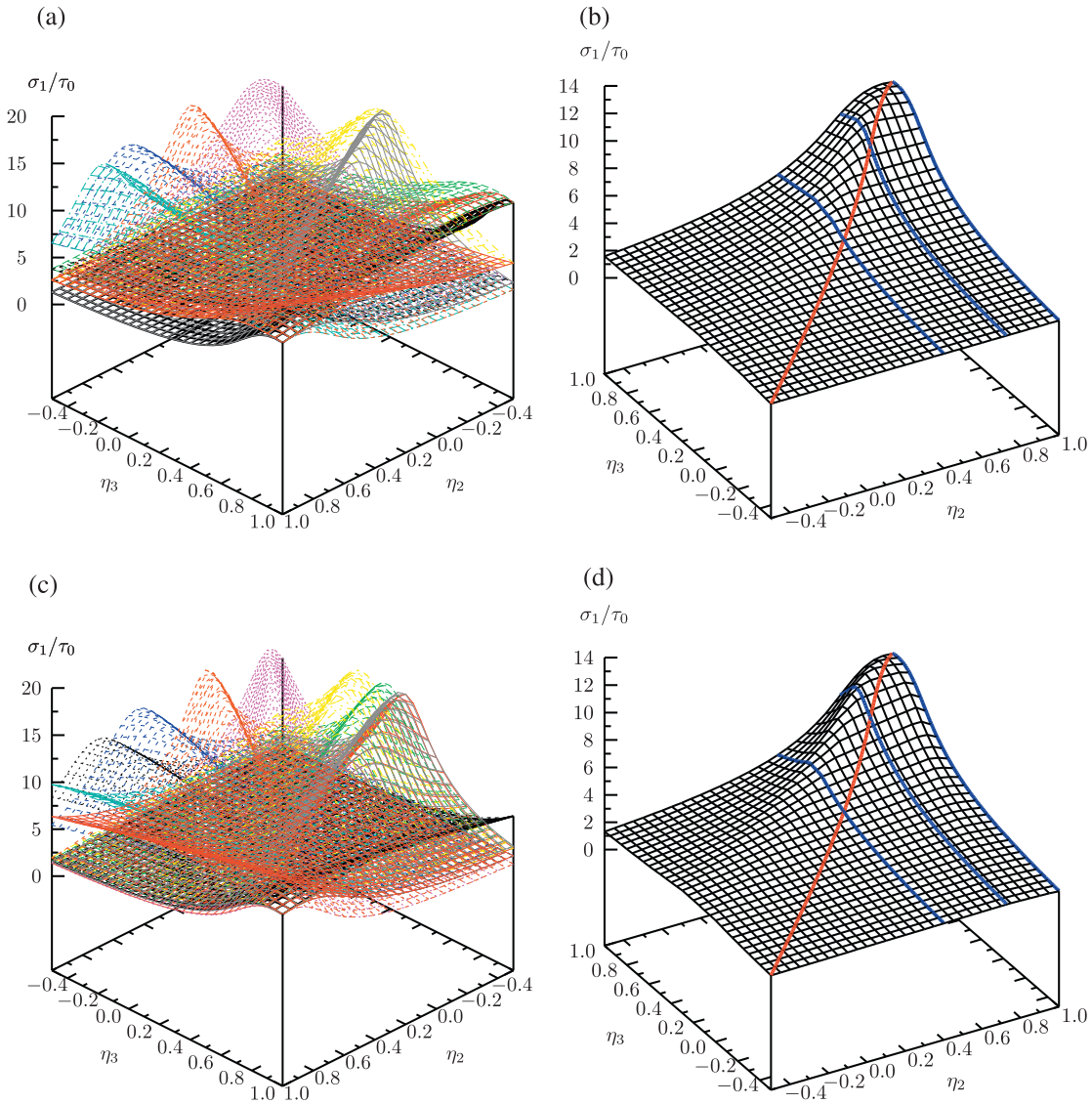

Fig. 13. [$\bar{1}$25] loading: (a) 3D yield surfaces for each slip system for **3** = [210], (b) 3D yield surface for the porous single crystal for **3** = [210], (c) 3D yield surfaces for each slip system for **3** = [(29)25], (d) 3D yield surface for the porous single crystal for **3** = [(29)25].

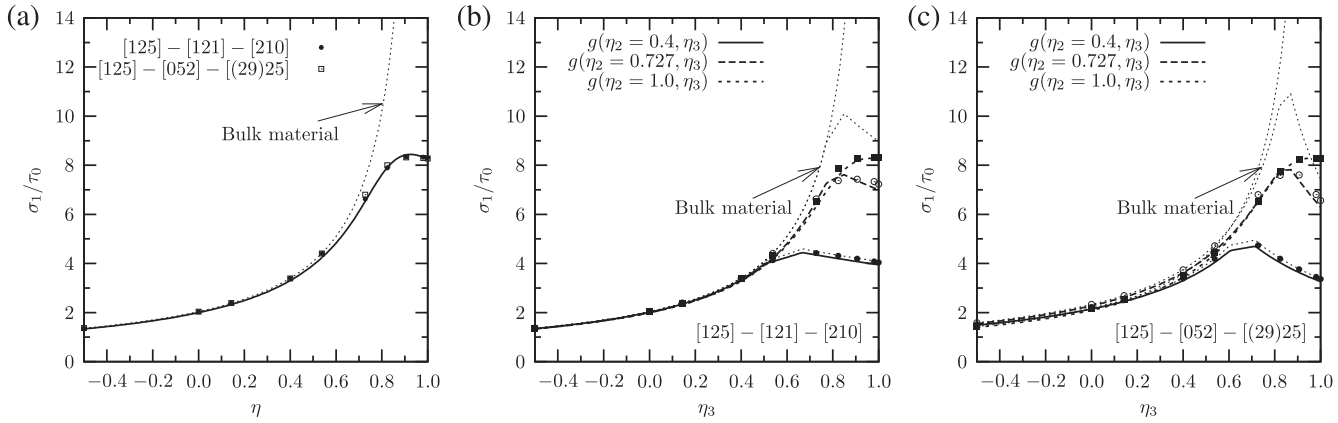

Fig. 14. Yield surfaces for the porous single crystal for $[\bar{1}25]$ loading, $f = 0.01$: (a) $\eta_2 = \eta_3 = \eta$ for $\mathbf{3} = [210]$ and $\mathbf{3} = [(29)25]$, (b) for $\mathbf{3} = [210]$ and $\eta_2 = 0.4, 0.727$ and 1, (c) for $\mathbf{3} = [(29)25]$ and $\eta_2 = 0.4, 0.727$ and 1.

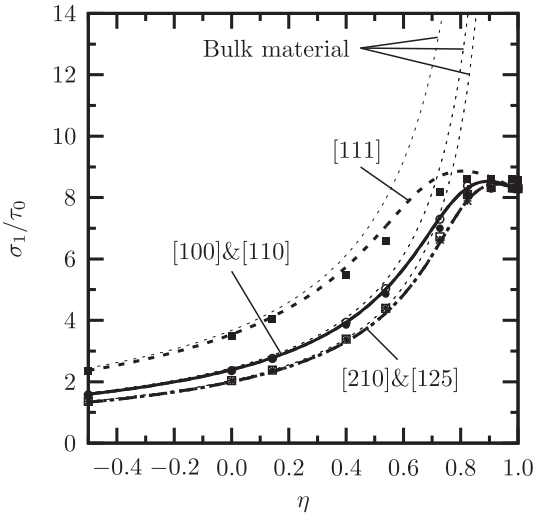

Fig. 15. Effect of the main loading direction **1** on the yield surface for the porous single crystal, in the case with $\eta_2 = \eta_3 = \eta$.$f = 0.01$.

the slip systems are obtained whereas for $\mathbf{3} = [(29)25]$ all 12 yield surfaces differ. The resulting theoretical yield surfaces are plotted in Figs. 13 for both secondary loading directions. Comparisons with FE results are shown in Fig. 14a for the $\eta_2 = \eta_3$ case, in Fig. 14b for various fixed values for η_2 and $\mathbf{3} = [210]$ and Fig. 14c for various fixed values for η_2 and $\mathbf{3} = [(29)25]$. The agreement between the model and the simulation results is excellent. Note, in particular, that the differences between $\mathbf{3} = [210]$ and $\mathbf{3} = [(29)25]$ at high stress triaxialities are well reproduced by the model (Figs. 14 a and c).

Yield surfaces in the particular case where $\eta_2 = \eta_3$ are compared in Fig. 15 for five different main loading directions. In that particular case results for $\mathbf{1} = [100]$ and $\mathbf{1} = [110]$ coincide as well as those for $\mathbf{1} = [210]$ and $\mathbf{1} = [\bar{1}25]$ as they share the same maximum Schmid factor. At low and moderate stress triaxialities the differences between the yield surfaces is controlled by the value of the Schmid factor for the bulk material. These differences tend to decrease at very high triaxiality levels. Under purely hydrostatic loads ($\eta \to 1$) the model predicts a unique yield stress σ_1 which is given by (solving Eq. 8 and Eq. 9 for $\tau_s = \sigma_{eq} = 0$ and $\sigma_m = \sigma_1$):

$$\frac{\sigma_1}{\tau_0} = \frac{1}{q_2}\sqrt{\frac{20}{3}}\operatorname{arccosh}\left(\frac{1+(q_1 f)^2}{2q_1 f}\right) \tag{24}$$

This limit is well verified by the FE simualtions.

4.5. Effect of void volume fraction f

The results presented above were obtained for a fixed porosity level (1%). In this section, the model and the unit cell calculations are compared for porosities equal to 0.5%, 1%, 2%, 5% and 10%. For the sake of conciseness, the comparison is limited to the case where $\eta_2 = \eta_3$ for a main loading direction equal to [100] (equivalent to [110] for $\eta_2 = \eta_3$), [111] or $[\bar{1}25]$ (equivalent to [210] for

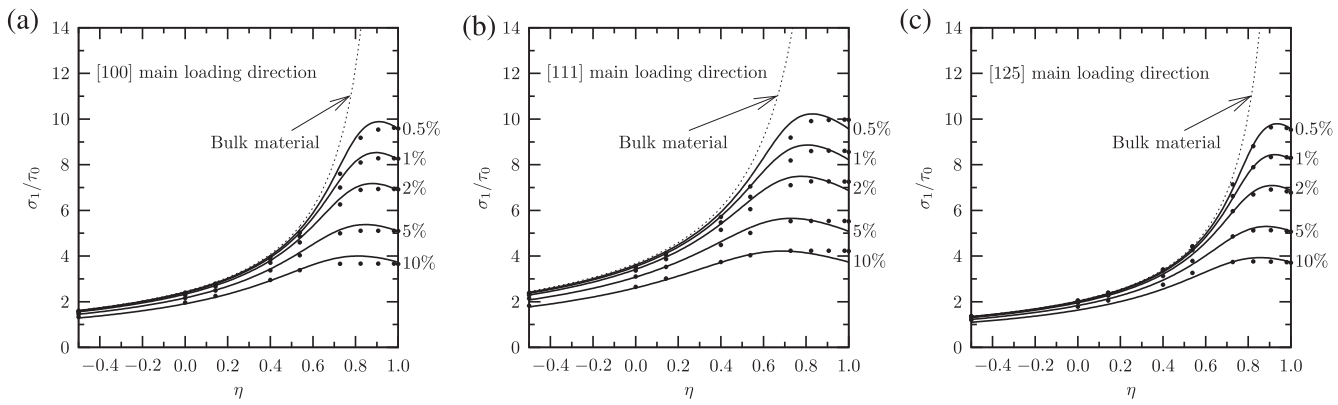

Fig. 16. Effect of porosity from 0.5% to 10% for various main loading directions, with $\eta_2 = \eta_3 = \eta$: (a) [100] main loading direction; (b) [111] main loading direction; (c) $[\bar{1}25]$ main loading direction.

$\eta_2 = \eta_3$). Results are shown in Fig. 16. Comparisons with results corresponding to the bulk material (thin dashed lines) are also presented. It is clearly observed that, for low triaxialities, the effect of porosity on the yield surface is rather limited so that yield surfaces for the voided materials are very close to the curve for the bulk material. Despite this moderate effect, FE simulations for these triaxiality and porosity ranges are needed to calibrate parameter α. The original model developed in Appendix A strongly underestimates the trends obtained using FE simulations with $\alpha = 1$ whereas the optimized value is much larger ($\alpha = 6.46$). At high triaxiality ratio, Eq. 24 appears to well represent FE simulations for the entire porosity range and all loading directions.

4.6. Field of plastic slip activation around the hole

The unit cell computations do no provide only results at the macroscopic scale but also fields of plastic deformation around the hole that bring information about the deformation modes of a hole in a single crystal. The impact of crystallography on the shape evolution of a hole in a single crystal matrix during growth was studied by Yerra et al. (2010) within the framework of finite deformation crystal plasticity. Since the limit analysis provided in the present work is limited to small strain, the shape changes are not illustrated here. Instead, maps are now provided showing the activation of slip systems around the hole depending on crystal orientation and prescribed stress triaxiality. For that purpose, the total cumulative slip γ_{cum} is defined as the sum of all the cumulative slip variables γ^s:

$$\gamma_{cum} = \sum_{s=1}^{12} \gamma^s \tag{25}$$

The field of total cumulative slip is illustrated in Fig. 17 for three different crystal orientations and three triaxiality levels for fixed values of porosity (1%) and mean strain. The pictures show middle cross-sections of the unit cell in the **1**–**2** plane, where 1 and 2 refer to the two first crystal directions indicated in the orientation of the cell. The inhomogeneity of plastic slip appears clearly in these maps with an obvious symmetry of the deformation patterns for the

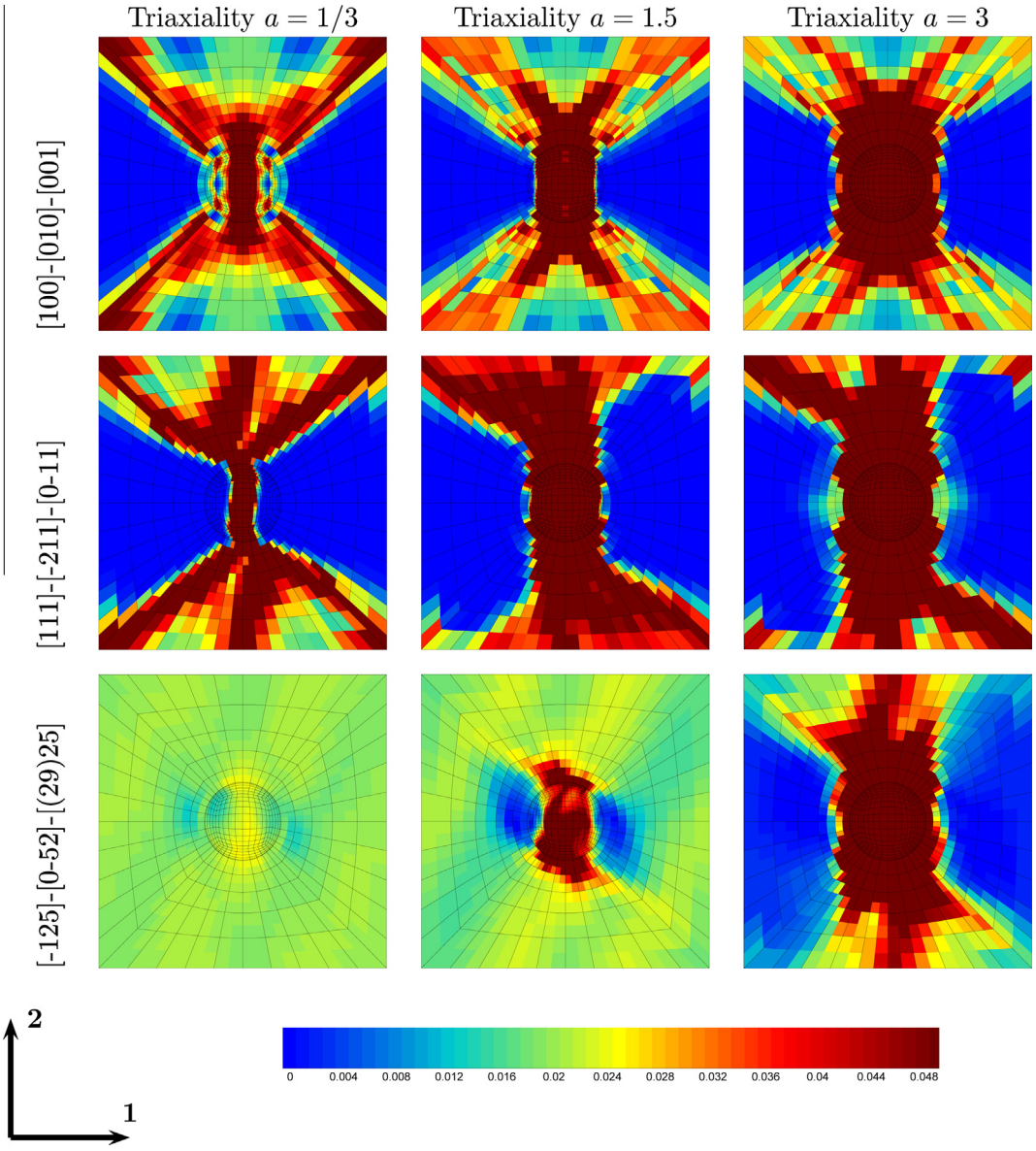

Fig. 17. Fields of cumulative plastic slip γ_{cum} on all slip systems in the **1**–**2** plane cross-section of the unit cell, shown on non-deformed meshes, for three different orientations and three different triaxialities for an overall plastic deformation $E^p_{11} = 0.01$. The porosity is $f = 0.01$.

[100] – [010] – [001] orientation, in contrast to the two other ones where symmetry is broken.

Fig. 18 shows the activation of the 12 slip systems around the hole in the case of an imposed triaxiality of 1.5, for the specific orientation [111] – [$\bar{2}$11] – [0$\bar{1}$1] with a given overall strain level. It turns out that all the slip systems are activated at some places, mainly around the North and South poles on the figure where multiple slip is observed. The fact that the twelve slip systems are activated at some place in the unit cell in contrast to the corresponding bulk single crystal is probably one reason why the von Mises equivalent stress must be introduced in the proposed yield function (Eq. 8) in addition to the resolved shear stress.

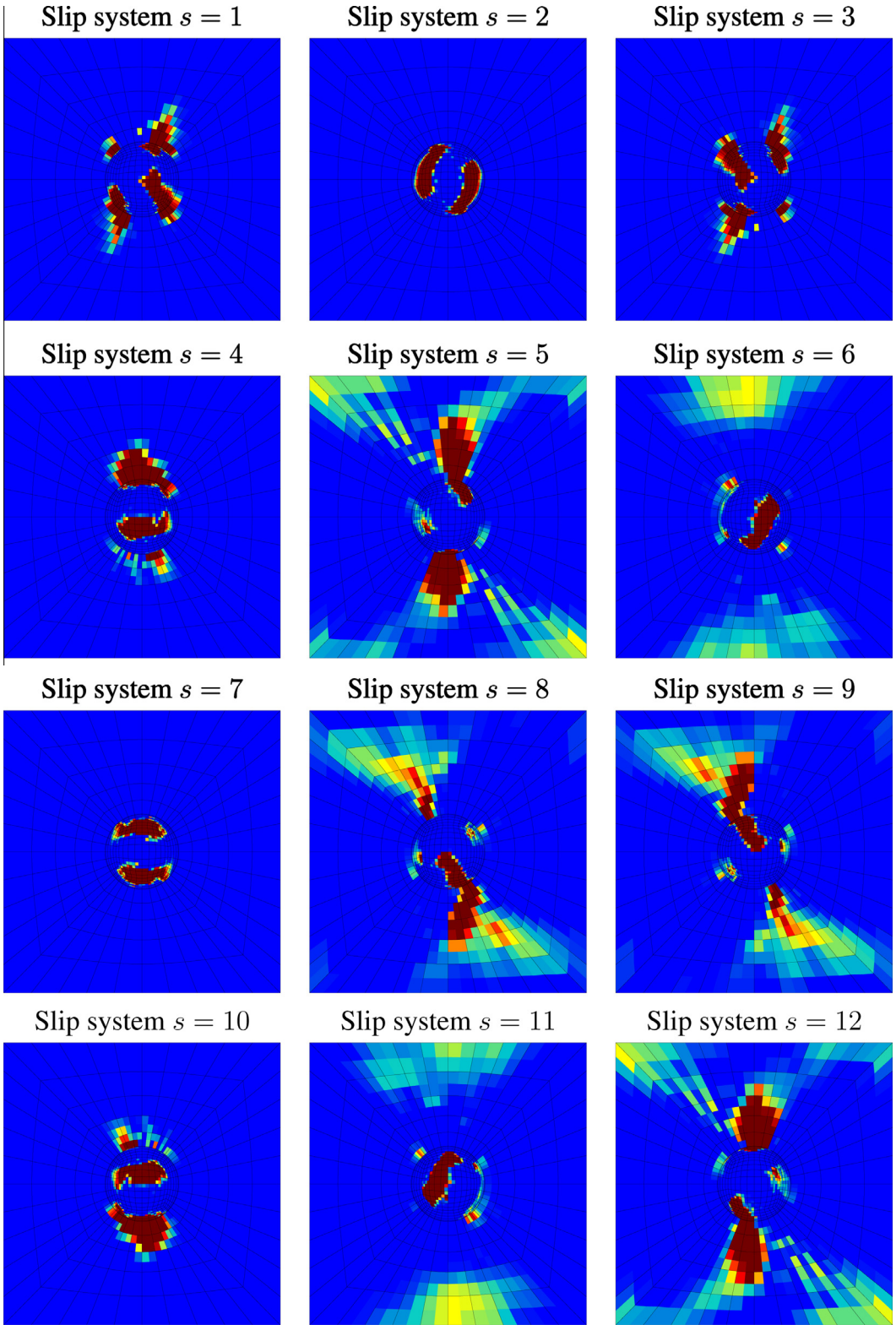

Fig. 18. Fields of the amount of slip γ^s on all slip systems in the **1–2** plane cross-section of the unit cell, for the orientation [111] – [$\bar{2}$11] – [0$\bar{1}$1] with an imposed triaxiality level of 1.5, shown on non-deformed meshes, for an overall plastic deformation $E^p_{11} = 0.01$. The porosity is $f = 0.01$. The color scale is the same as in Fig. 17.

5. Conclusion

The original contribution of the present work to the modeling of ductile fracture in single crystals is to provide a yield function in closed form for porous single crystals and to validate it by means of systematic unit cell computations. It is theoretically motivated using a variational micromechanical approach. It is formulated as the combination of N yield criteria, N being the number of potential slip systems in the single crystal matrix, based on the definition of a new effective equivalent stress measure for each slip system. This equivalent stress measure incorporates in a nonlinear way the resolved shear stress on the considered slip system and the equivalent von Mises and mean stresses. To better match an exponential dependence on the mean stress (which is well recognized for rate-independent materials), this yield function was phenomenologically extended following a procedure similar to the GTN extension of Gurson's model (Tvergaard and Needleman, 1984 and Leblond et al., 1994). The extension introduces three adjustable parameters (q_1, q_2 and α). Unit cell simulations were used to fit these parameters in the case of a FCC single crystal. Various stress triaxiality ratios, main loading directions and porosity levels were considered for the unit cell simulations. In all cases, the model was able to capture the results of the calculations with a very good accuracy, including the effects of main loading direction, of secondary loading direction and of porosity.

Further work will include the analysis of the plastic flow rule associated with the proposed yield function. In particular, the validity of the normality rule Eq. 10 will be tested for this new yield criterion. In addition, the porosity growth rate ($\dot{f} = (1-f)\mathrm{trace}(\underline{\dot{\varepsilon}}_p)$) will be investigated by comparing the results of the model and unit cell simulations. It is well-known that crystallographic aspects of plastic deformation around holes strongly affect their growth rate, for example in H.C.P. metals, see Crépin et al. (1996). The proposed yield function will then be used to develop a set of constitutive equations for the porous single crystal including self and cross-hardening within a finite strain framework. A first application of this model will be the evaluation of the fracture toughness properties in presence of swelling in irradiated stainless steels.

Appendix A. Development of a model for voided viscous single crystals

In this section a model is developed for viscous single crystals containing spherical voids. The single crystal is assumed to have a nonlinear viscous behaviour with N slip systems. Following DeBotton and Ponte Castañeda (1995) each slip system is associated to a slip potential function ϕ_s defined as:

$$\phi_s = \frac{\dot{\gamma}_0 \tau_0}{n+1}\left|\frac{\tau_s}{\tau_0}\right|^{n+1} \tag{A.1}$$

where $\dot{\gamma}_0 (>0)$ and $\tau_0 (>0)$, respectively, are the reference slip rate and the reference flow stress of slip system s. The creep exponent is denoted by n and τ^s is the resolved shear stress on the slip system s, given by:

$$\tau_s = \underline{\sigma} : \underline{m}_s \tag{A.2}$$

where $\underline{m}_s$ is the orientation tensor defined by Eq. 1. The overall stress potential of the single crystal is the sum of the potentials for all slip systems:

$$\Phi(\underline{\sigma}) = \sum_{s=1}^{N} \phi_s(\tau_s) \tag{A.3}$$

As defined in Eq. A.1, ϕ_s is a power law function which is strictly convex.

Based on the work by DeBotton and Ponte Castañeda (1995), a stress potential for a linear comparison single crystal is introduced as:

$$\Phi_L(\underline{\sigma}) = \frac{1}{2}\underline{\sigma} : \mathbb{M}^{\chi} : \underline{\sigma} = \sum_{s=1}^{N} \alpha_s \tau_s^2 \tag{A.4}$$

where α_s denotes the slip system compliance. The fourth-order compliance tensor is written as:

$$\mathbb{M}^{\chi} = 2\sum_{s=1}^{N} \alpha_s \underline{m}_s \otimes \underline{m}_s = 2\sum_{s=1}^{N} \alpha_s \mathbb{R}_s \tag{A.5}$$

Then, according to DeBotton and Ponte Castañeda (1995) dual potentials are defined as:

$$\phi_s(\tau_s) = \max_{\alpha_s \geqslant 0}\{\alpha_s \tau_s^2 - V_s(\alpha_s)\} \tag{A.6}$$

$$V_s(\alpha_s) = \max_{\tau_s \geqslant 0}\{\alpha_s \tau_s^2 - \phi_s(\tau_s)\} \tag{A.7}$$

Using Eq. A.1 together with Eq. A.7, by taking account of the convexity of the viscous potential with $n > 1$, the function V_s can be explicitly expressed as:

$$V_s(\alpha_s) = \frac{n-1}{n+1}\frac{\dot{\gamma}_0 \tau_0}{2}\left(\frac{2\tau_0 \alpha_s}{\dot{\gamma}_0}\right)^{\frac{n+1}{n-1}} \tag{A.8}$$

Based on this constitutive model for the single crystal, the porous single crystal can be further described introducing a variational characterization as proposed in Ponte Castañeda (1991); Ponte Castañeda(1992a). The effective stress potential for the "composite" (i.e. single crystal + voids) is derived from the theorem of minimum complementary potential energy, by the following relation:

$$\overline{\Phi}(\underline{\Sigma}) = \min_{\underline{\sigma}(\vec{x}) \in \boldsymbol{S}} \int_{\Omega} \Phi(\underline{\sigma}(\vec{x}))\, d\Omega \tag{A.9}$$

with Ω being the representative volume element containing voids and the metallic matrix, $\underline{\Sigma}$ the macroscopic stress tensor defined as the average over the total volume $\underline{\Sigma} = \langle \underline{\sigma}(\vec{x}) \rangle_{\Omega}$, and $\boldsymbol{S}$ the set of Statically Admissible (S.A.) stress fields with a homogeneous stress boundary condition on the outer boundary $\partial\Omega$ of $\Omega : \underline{\sigma}(\vec{x})$ S.A. $\Longleftrightarrow \underline{\sigma} \in \boldsymbol{S}$ with $\boldsymbol{S} = \{\mathrm{div}(\underline{\sigma}) = \vec{0}$ in Ω and $\underline{\sigma}.\vec{n} = \underline{\Sigma}.\vec{n}$ on $\partial\Omega\}$ where $\vec{n}$ is the outer normal to the boundary, $\partial\Omega$, of Ω.

Following Ponte Castañeda (1992b) and Ponte Castañeda and Zaidman (1996), the effective potential can be estimated as:

$$\overline{\Phi}(\underline{\Sigma}) \geqslant \max_{\{\alpha_r \geqslant 0\}_{r=1,N}} \left(\overline{\Phi}_L(\underline{\Sigma}) - (1-f)\sum_{s=1}^{N} V_s(\alpha_s)\right) \tag{A.10}$$

where $\overline{\Phi}_L(\underline{\Sigma})$ denotes any estimate of the potential of the linear composite. $\overline{\Phi}_L$ can be expressed as:

$$\overline{\Phi}_L(\underline{\Sigma}) = \frac{1}{2}\underline{\Sigma} : \overline{\mathbb{M}} : \underline{\Sigma} \tag{A.11}$$

where $\overline{\mathbb{M}}$ is an estimate of the effective viscous compliance fourth order tensor of the "composite". In Eq. A.10 it has been assumed that the slip system compliance α_s can be considered as identical for each slip system of the single crystal and independent of the position in Ω. Furthermore, the $(1-f)$ factor accounts for the fact that only a fraction of the composite corresponds to the single crystal. The remainder (i.e. f) corresponds to voids for which the V function is equal to zero.

In the following, Eq. A.10 will be regarded as an equality in order to obtain an estimate of the potential of the composite (Ponte Castañeda and Zaidman, 1996). To proceed it is also necessary to select a proper estimate of the effective stress potential of the linear comparison single crystal ($\overline{\Phi}_L$). In the following a Hashin–Shtrikman lower bound will be used. In that case the effective

viscous compliance tensor $\overline{\mathbb{M}}$ (referred to as $\overline{\mathbb{M}}^{\mathrm{HS}-}$) is given by the following equation (DeBotton and Ponte Castañeda, 1995):

$$\left[\overline{\mathbb{M}}^{\mathrm{HS}-}+\mathbb{M}^{*}\right]^{-1}=(1-f)\left[\mathbb{M}^{\chi}+\mathbb{M}^{*}\right]^{-1}+f\left[\mathbb{M}^{\mathrm{v}}+\mathbb{M}^{*}\right]^{-1} \tag{A.12}$$

where $\mathbb{M}^{\mathrm{v}}$ is the compliance tensor of the voids. $\mathbb{M}^{*}$ is the inverse of the influence tensor of Hill for a spherical void. As the bulk and shear moduli of the void are equal to zero, Eq. A.12 leads to:

$$\overline{\mathbb{M}}^{\mathrm{HS}-}=\frac{1}{1-f}\mathbb{M}^{\chi}+\frac{f}{1-f}\mathbb{M}^{*} \tag{A.13}$$

The inverse of the influence tensor of Hill can easily be computed in the case of an isotropic compliance matrix which is expressed as [1]:

$$\mathbb{M}_{0}=\frac{1}{3\kappa_{0}}\mathbb{J}+\frac{1}{2\mu_{0}}\mathbb{K} \tag{A.14}$$

In the case where the matrix material can be considered as incompressible (i.e. $\kappa_0\to\infty$), the tensor $\mathbb{M}^{*}$ is found to be:

$$\mathbb{M}^{*}=\frac{1}{4\mu_{0}}\mathbb{J}+\frac{1}{3\mu_{0}}\mathbb{K}\equiv\frac{1}{3\kappa^{*}}\mathbb{J}+\frac{1}{2\mu^{*}}\mathbb{K} \tag{A.15}$$

In the following $\mathbb{M}_0$ (defined by the shear modulus μ_0 only) will be used instead of $\mathbb{M}^{\chi}$ to compute $\mathbb{M}^{*}$, since no direct expression for $\mathbb{M}^{*}$ as a function of $\mathbb{M}^{\chi}$ is available. A suitable value for μ_0 must consequently be used. In that case the lower bound character of the model is lost. As a first approximation, it is assumed that the deviatoric projections of $\mathbb{M}^{\chi}$ and $\mathbb{M}_0$ are equal so that:

$$\mathbb{M}^{\chi}::\mathbb{K}=\mathbb{M}_{0}::\mathbb{K} \tag{A.16}$$

Noting that $\mathbb{K}::\mathbb{K}=5$ and that $\mathbb{R}_s::\mathbb{K}=\frac{1}{2},\forall s$, one finally obtains from A.5 and A.14:

$$\mu_{0}=\frac{5}{2\sum_{s}\alpha_{s}} \tag{A.17}$$

Using relation A.13, the effective stress potential of the porous linear comparison single crystal can be approximated as:

$$\begin{aligned}\overline{\Phi}_{L}(\underline{\Sigma})&=\frac{1}{2}\underline{\Sigma}:\overline{\mathbb{M}}^{\mathrm{HS}}-:\underline{\Sigma}=\frac{1}{2}\underline{\Sigma}:\left(\frac{1}{1-f}\mathbb{M}^{\chi}+\frac{f}{1-f}\mathbb{M}^{*}\right):\underline{\Sigma}\\&=\frac{1}{1-f}\left(\sum_{s}\alpha_{s}T_{s}^{2}+f\overline{\Phi}^{*}(\underline{\Sigma})\right)\end{aligned} \tag{A.18}$$

where $T_s=\underline{\Sigma}:\underline{m}^{s}$ is the macroscopic resolved shear stress of the slip system s for the non-linear single crystal and $\overline{\Phi}^{*}(\underline{\Sigma})$ is derived from A.11 and A.15:

$$\overline{\Phi}^{*}(\underline{\Sigma})=\frac{1}{2\kappa^{*}}\Sigma_{m}^{2}+\frac{1}{6\mu^{*}}\Sigma_{eq}^{2} \tag{A.19}$$

where Σ_m (resp. Σ_{eq}) is the mean stress (resp. von Mises stress) of the macroscopic stress tensor $\underline{\Sigma}$. Note that $\overline{\Phi}^{*}$ is expressed using isotropic invariants of $\underline{\Sigma}$ because $\mathbb{M}_0$ is assumed to be isotropic as a first approximation. Finally $\overline{\Phi}_L$ can be expressed as:

$$\overline{\Phi}_{L}(\underline{\Sigma})=\frac{1}{1-f}\sum_{s=1}^{N}\left\{\alpha_{s}\left[T_{s}^{2}+f\left(\frac{3}{20}\Sigma_{m}^{2}+\frac{2}{45}\Sigma_{eq}^{2}\right)\right]\right\} \tag{A.20}$$

It follows that the estimate of the effective potential $\overline{\Phi}$ can be rewritten using A.10 and A.8 as:

$$\begin{aligned}\overline{\Phi}(\underline{\Sigma})=\max_{\{\alpha_r\geqslant 0\}_{r=1,N}}\Bigg[&\frac{1}{1-f}\sum_{s=1}^{N}\left(\alpha_{s}\left(T_{s}^{2}+f\left(\frac{3}{20}\Sigma_{m}^{2}+\frac{2}{45}\Sigma_{eq}^{2}\right)\right)\right)\\&-(1-f)\sum_{s=1}^{N}\frac{n-1}{n+1}\frac{\dot{\gamma}_{0}\tau_{0}}{2}\left(\frac{2\tau_{0}\alpha_{s}}{\dot{\gamma}_{0}}\right)^{\frac{n+1}{n-1}}\Bigg]\end{aligned} \tag{A.21}$$

At this stage of the derivation it is convenient to introduce the following quantity:

$$T_{s}^{*}=\frac{1}{1-f}\left(T_{s}^{2}+f\left(\frac{2}{45}\Sigma_{eq}^{2}+\frac{3}{20}\Sigma_{m}^{2}\right)\right)^{\frac{1}{2}} \tag{A.22}$$

In order to maximize the right hand-side of Eq. A.21 one needs to solve the system of equations formed by the vanishing of the partial derivatives of the argument of the Max operator in (A.21) with respect to $\alpha_s,\forall s$. This leads to:

$$\alpha_{s}=\frac{\dot{\gamma}_{0}}{2\tau_{0}}\left(\frac{T_{s}^{*}}{\tau_{0}}\right)^{n-1} \tag{A.23}$$

Introducing this solution into Eq. A.21 leads to the following expression for $\overline{\Phi}$:

$$\overline{\Phi}(\underline{\Sigma})=(1-f)\sum_{s}\frac{\dot{\gamma}_{0}\tau_{0}}{n+1}\left|\frac{T_{s}^{*}}{\tau_{0}}\right|^{n+1}\equiv\sum_{s}\overline{\phi}_{s}(T_{s}^{*}) \tag{A.24}$$

Based on this equation, effective slip systems can be attributed to the homogenized porous single crystal whereby T_s^* can be interpreted as an effective scalar resolved stress acting on each slip system. Rate independent plasticity is obtained for $n\to+\infty$. The yield surface for each slip system is then expressed as: $T_s^*-\tau_0=0$.

[1] $\mathbb{J}$ and $\mathbb{K}$ are fourth order tensors such that: $\mathbb{J}:\underline{a}=\frac{1}{3}a_{kk}\underline{1}$ and $\mathbb{K}:\underline{a}=\underline{a}-\frac{1}{3}a_{kk}\underline{1}$ (deviator of $\underline{a}$) for any second order tensor $\underline{a}$.

References

Bandstra, J., Koss, D., 2008. On the influence of void clusters on void growth and coalescence during ductile failure. Acta Mater. 56, 4429–4439.

Benzerga, A.A., Besson, J., 2001. Plastic potentials for anisotropic porous solids. Eur. J. Mech./A 20 (3), 397–434.

Benzerga, A., Leblond, J., 2010. Ductile fracture by void growth to coalescence. Adv. Appl. Mech. 44, 169–305.

Benzerga, A., Besson, J., Pineau, A., 2004. Anisotropic ductile fracture. Part II: Theory. Acta Metall. 52, 4639–4650.

Besson, J., 2010. Continuum models of ductile fracture: a review. Int. J. Damage Mech. 19 (1), 3–52.

Besson, J., Foerch, R., 1998. Application of object-oriented programming techniques to the finite element method. Part I: General concepts. Revue Europenne des Elements Finis 7 (5), 535–566.

Besson, J., Steglich, D., Brocks, W., 2001. Modeling of crack growth in round bars and plane strain specimens. Int. J. Solids Struct. 38 (46–47), 8259–8284.

Besson, J., Cailletaud, G., Chaboche, J.-L., Forest, S., Blétry, M., 2009. Non-Linear Mechanics of Materials. Series: Solid Mechanics and Its Applications, vol. 167. Springer.

Brocks, W., Sun, D.Z., Honig, A., 1995. Verification of the transferability of micromechanical parameters by cell model calculations with visco-plastic materials. Int. J. Plasticity 11 (8), 971–989.

Crépin, J., Bretheau, T., Caldemaison, D., 1996. Cavity growth and rupture of β–treated zirconium: a crystallographic model. Acta Mater. 44, 4927–4935.

Danas, K., Ponte Castañeda, P., 2009. A finite-strain model for anisotropic viscoplastic porous media: I-Theory. Eur. J. Mech. A/Solids 28, 387–401.

DeBotton, G., Ponte Castañeda, P., 1995. Variational estimates for the creep behaviour of polycrystals. Proc. R. Soc. London Ser. A-Math. Phys. Sci. 448, 121–142.

Dubuisson, P., 2011. Le gonflement des aciers austénitiques. Revue de Métallurgie 108, 33–37.

Fabrègue, D., Pardoen, T., 2008. A constitutive model for elastoplastic solids containing primary and secondary voids. J. Mech. Phys. Solids 56, 719–741.

Faleskog, J., Shih, C., 1997. Micromechanics of coalescence — I. Synergistic effects of elasticity, plastic yielding and multi-size-scale voids. J. Mech. Phys. Solids 45 (1), 21–50.

Faleskog, J., Gao, X., Shih, C., 1998. Cell model for nonlinear fracture analysis — I. Micromechanics calibration. Int. J. Frac. 89, 355–373.

Foerch, R., Besson, J., Cailletaud, G., Pilvin, P., 1997. Polymorphic constitutive equations in finite element codes. Comput. Methods Appl. Mech. Eng. 141, 355–372.

Foster, J.P., Strain, R.V., 1974. Empirical swelling equations for solution-annealed type 304 stainless steel. Nucl. Technol., 93–98.

Fritzen, F., Forest, S., Boehlke, T., Kondo, D., Kanit, T., 2012. Computational homogenization of elasto-plastic porous metals. Int. J. Plasticity 29, 102–119.

Gan, Y., Kysar, J., 2007. Cylindrical void in a rigid-ideally plastic single crystal III: hexagonal close-packed crystal. Int. J. Plasticity 23 (4), 592–619.
Gan, Y., Kysar, J., Morse, T., 2006. Cylindrical void in a rigid-ideally plastic single crystal II: experiments and simulations. Int. J. Plasticity 22, 39–72.
Gao, X., Faleskog, J., Shih, C., 1998. Cell model for nonlinear fracture analysis — ii. fracture–process calibration and verification. Int. J. Fract. 89, 375–398.
Goldstein, H., Poole, C., Safko, J., 2002. Classical Mechanics, third Ed. Addison Wesley.
Gologanu, M., Leblond, J.-B., 1993. Approximate models for ductile metals containing non-spherical voids - Case of axisymmetric prolate ellipsoidal cavities. J. Mech. Phys. Solids 41, 1723–1754.
Gurson, A., 1977. Continuum theory of ductile rupture by void nucleation and growth: part I— Yield criteria and flow rules for porous ductile media. J. Eng. Mater. Technol. 99, 2–15.
Ha, S., Kim, K., 2010. Void growth and coalescence in F.C.C. single crystals. Int. J. Solids Struct. 52 (7), 863–873.
Huang, M., Li, Z., Wang, C., 2007. Discrete dislocation dynamics modelling of microvoid growth and its intrinsic mechanism in single crystals. Acta Mater. 55, 1387–1396.
Huang, M., Zhao, L., Tong, J., 2012. Discrete dislocation dynamics modelling of mechanical deformation of nickel-based single crystal superalloys. Int. J. Plasticity 28, 141–158.
Hussein, M., Borg, U., Niordson, C., Deshpande, V., 2008. Plasticity size effects in voided crystals. J. Mech. Phys. Solids 56, 114–131.
Koplik, J., Needleman, A., 1988. Void growth and coalescence in porous plastic solids. Int. J. Solids Structures 24 (8), 835–853.
Kuna, M., Sun, D.Z., 1996. Three-dimensional cell model analyses of void growth in ductile materials. Int. J. Fract. 81 (3), 235–258.
Kysar, J., Gan, Y., Mendez-Arzuza, G., 2005. Cylindrical void in a rigid-ideally plastic single crystal. Part I: Anisotropic slip line theory solution for face-centered cubic crystals. Int. J. Plasticity 21 (8), 1481–1520.
Lebensohn, R., Idiart, M., Ponte Castañeda, P., Vincent, P.-G., 2011. Dilatational viscoplasticity of polycrystalline solids with intergranular cavities. Philos. Mag. 91 (22), 3038–3067.
Leblond, J., Perrin, G., Suquet, P., 1994. Exact results and approximate models for porous viscoplastic solids. Int. J. Plasticity 10 (3), 213–235.
Lecarme, L., Tekoğlu, C., Pardoen, T., 2011. Void growth and coalescence in ductile solids with stage III and stage IV strain hardening. Int. J. Plasticity 27 (8), 1203–1223.
Liu, Y., Gilormini, P., Ponte Castañeda, P., 2005. Homogenization estimates for texture evolution in halite. Tectonophysics 406, 179–195.
Liu, W.H., Zhang, X.M., Tang, J.G., Du, Y.X., 2007. Simulation of void growth and coalescence behavior with 3d crystal plasticity theory. Comput. Mater. Sci. 40 (1), 130–139.
Liu, W., Huang, H., Tang, J., 2010. FEM simulation of void coalescence in FCC crystals. Comput. Mater. Sci. 50, 411–418.
Liu, W., He, Z., Tang, J., Hu, Z., Cui, D., 2012. The effects of load condition on void coalescence in FCC single crystals. Comput. Mater. Sci. 60, 66–74.
Mc Clintock, F., 1968. A criterion for ductile fracture by the growth of holes. J. App. Mech. 35, 363–371.
Monchiet, V., Charkaluk, E., Kondo, D., 2007. An improvement of gurson-type models of porous materials by using eshelby-like trial velocity fields. C.R. Acad. Sci. Paris 335 (1), 32–41.
Monchiet, V., Cazacu, O., Charkaluk, E., Kondo, D., 2008. Macroscopic yield criteria for plastic anisotropic materials containing spheroidal voids. Int. J. Plasticity 24, 1158–1189.
Needleman, A., 1972. Void growth in an elastic-plastic medium. J. Appl. Mech. 39 (4), 964–970.
Pardoen, T., Hutchinson, J.W., 2000. An extended model for void growth and coalescence. J. Mech. Phys. Solids 48 (12), 2467–2512.
Pineau, A., Pardoen, T., 2007. Failure mechanisms of metals. Elsevier (Chapter 6).
Ponte Castañeda, P., 1991. The effective mechanical properties of nonlinear isotropic composites. J. Mech. Phys. Solids 39 (1), 45–71.
Ponte Castañeda, P., 1992a. New variational principles in plasticity and their application to composite materials. J. Mech. Phys. Solids 40 (8), 1757–1788.
Ponte Castañeda, P., 1992b. A new variational principle and its application to nonlinear heterogeneous systems. SIAM J. Appl. Math. 52 (5), 1321–1341.
Ponte Castañeda, P., Suquet, P., 1998. Nonlinear composites. Adv. Appl. Mech. 34, 171–302.
Ponte Castañeda, P., Zaidman, M., 1996. The finite deformation of nonlinear composite materials. I: Instantaneous constitutive relations. Int. J. Solids Struct. 33 (9), 1271–1286.
Potirniche, G., Horstemeyer, M., Wagner, G., Gullett, P., 2006. A molecular dynamics study of void growth and coalescence in single crystal nickel. Int. J. Plasticity 22, 257–278.
Quinn, D.F., Connolly, P.J., Howe, M.A., McHugh, P.E., 1997. Simulation of void growth in wc-co hardmetals using crystal plasticity theory. Int. J. Mech. Sci. 39 (2), 173–183.
Renault, A., Malaplate, J., Pokor, C., Gavoille, P., 2011. TEM and EFTEM characterization of solution annealed 304l stainless steel irradiated in PHENIX, up to 36 dpa and at 390°C. J. Nucl. Mater. 421, 124–131.
Rice, J., Tracey, D., 1969. On the ductile enlargement of voids in triaxial stress fields. J. Mech. Phys. Solids 17, 201–217.
Schacht, T., Untermann, N., Steck, E., 2003. The influence of crystallographic orientation on the deformation behaviour of single crystals containing microvoids. Int. J. Plasticity 19, 1605–1626.
Segurado, J., Llorca, J., 2009. An analysis of the size effect on void growth in single crystals using discrete dislocation dynamics. Acta Mater. 57, 1427–1436.
Segurado, J., Llorca, J., 2010. Discrete dislocation dynamics analysis of the effect of lattice orientation on void growth in single crystals. Int. J. Plasticity 26, 806–819.
Seran, J., Le Naour, L., Grosjean, P., Hugon, M., Carteret, Y., Maillard, A., 1984. Swelling and microstructure of neutron-irradiated Ti-modified type 316 stainless steel. In: Proc. of the 12th Int. Conf. on Effects of Radiation on Materials (Williamsburg 1984), ASTM STP 870, pp. 233–247.
Steglich, D., Brocks, W., 1997. Micromechanical modelling of the behaviour of ductile materials including particles. Comput. Mater. Sci. 9, 7–17.
Steglich, D., Siegmund, T., Brocks, W., 1999. Micromechanical modeling of damage due to particle cracking in reinforced metals. Comput. Mater. Sci. 16, 404–413.
Tang, T., Kim, S., Horstemeyer, M., 2010a. Fatigue crack growth in magnesium single crystals under cyclic loading: molecular dynamics simulation. Comput. Mater. Sci. 48, 426–439.
Tang, T., Kim, S., Horstemeyer, M., 2010b. Molecular dynamics simulations of void growth and coalescence in single crystal magnesium. Acta Mater. 58, 4742–4759.
Traiviratana, S., Bringa, E., Benson, D., Meyers, M., 2008. Void growth in metals: atomistic calculations. Acta Mater. 56, 3874–3886.
Tvergaard, V., 1981. Influence of voids on shear band instabilities under plane strain conditions. Int. J. Fract. 17 (4), 389–407.
Tvergaard, V., 1982. On localization in ductile materials containing spherical voids. Int. J. Fract. 18 (4), 237–252.
Tvergaard, V., Needleman, A., 1984. Analysis of the cup–cone fracture in a round tensile bar. Acta Metall. 32, 157–169.
Wang, Y., Yue, Z., Stein, M., 2006. Experimental and finite element study of void growth in nickel-base single crystal superalloys. Rare Metal Mater. Eng. 35 (1), 39–42.
Worswick, M.J., Pick, R.J., 1990. Void growth and constitutive softening in a periodically voided solid. J. Mech. Phys. Solids 38 (5), 601–625.
Yerra, S.K., Tekoglu, C., Scheyvaerts, F., Delannay, L., van Houtte, P., Pardoen, T., 2010. Void growth and coalescence in single crystals. Int. J. Solids Struct. 47 (7-8), 1016–1029.
Yu, Q.M., Hou, N.X., Yue, Z.F., 2010. Finite element analysis of void growth behavior in nickel-based single crystal superalloys. Comput. Mater. Sci. 48 (3), 597–608.
Zhang, K.S., Bai, J.B., François, D., 1999. Ductile fracture of materials with high void volume fraction. Int. J. Solids Struct. 36 (23), 3407–3425.
Zhao, K., Chen, C., Shen, Y., Lu, T., 2009. Molecular dynamics study on the nano-void growth in face-centered cubic single crystal copper. Comput. Mater. Sci. 46, 749–754.